Stem Cell Reviews and Reports (2026) 22:1420–1441
https://doi.org/10.1007/s12015-026-11061-4

RESEARCH

Human Myelin Spheres for in Vitro Oligodendrocyte Maturation, Myelination and Neurological Disease Modeling

Karan Ahuja[1] · Roya Ramezankhani[1] · Xinyu Wang[2] · Thibaut Burg[3] · Giulia Amos[4] · Katrien Neyrinck[1] · Alessio Silva[3] · Geethika Arekatla[3] · Eleanor Eva Cassidy[1] · Fatemeharefeh Nami[1] · Joke Terryn[1] · Keimpe Wierda[5] · Katlijn Vints[6] · Niels Vandamme[7] · Suresh Poovathingal[8] · Ivo Lambrichts[9] · Johannes V. Swinnen[10] · Ludo Van Den Bosch[3] · Lies De Groef[11] · Lieve Moons[12] · Catherine Verfaillie[1] · Johan Neyts[2] · Dirk Jochmans[2] · Yoke Chin Chai[1,13]

Received: 14 November 2025 / Accepted: 7 January 2026 / Published online: 28 January 2026

Abstract
Demyelinating diseases, such as multiple sclerosis, damage the protective myelin sheaths of the central nervous system. The development of effective therapies has been hampered by the lack of models that accurately replicate human myelin biology. Here we present a novel method to generate human myelin spheres (MyS) by coculturing of hPSC-derived neuronal and oligodendrocyte precursor cells, to create myelinated neurons. Using multimodal analyses including confocal and (electron)microscopy, single-nuclei transcriptomics, lipidomics, and electrophysiology, we demonstrate myelination in MyS as early as six weeks into coculture. These myelinated structures mature over time into multilamellar and compacted myelin sheaths with lipid compositions and transcriptomic profiles mirror the temporal dynamics of in vivo human oligodendrocyte development and neuronal myelination, resembling those of late fetal oligodendrocytes. By employing lysolecithin-induced demyelination and Rabies virus infection experiments, we demonstrate the potential of MyS as an innovative, physiologically relevant platform for studying myelin-related neurodegeneration and neuroinfection.

Co-first authorship Karan Ahuja and Roya Ramezankhani.

✉ Yoke Chin Chai
Yoke.Chin.Chai@imec.be

[1] Stem Cell Institute Leuven, Department of Development and Regeneration, KU Leuven, O&N4, Herestraat 49, Leuven 3000, Belgium

[2] Virology, Antiviral Drug & Vaccine Research Group, Department of Microbiology, Immunology and Transplantation, Rega Institute, KU Leuven, Leuven, Belgium

[3] VIB Center for Brain & Disease Research, Laboratory of Neurobiology, VIB-KU Leuven, Leuven, Belgium

[4] Institute for Biomedical Engineering, ETH Zurich, Zurich 8092, Switzerland

[5] VIB-KU Leuven Center for Brain & Disease Research Technologies, Electrophysiology, Leuven, Belgium

[6] Bio Imaging Core, VIB-KU Leuven Center for Brain & Disease Research, Leuven 3000, Belgium

[7] VIB Single Cell Core, VIB, VIB-KU Leuven Center for Cancer Biology, Leuven, Belgium

[8] VIB-KU Leuven Center for Brain and Disease Research Technologies, Single Cell, Microfluidics and Bioinformatics Expertise Units, Leuven, Belgium

[9] Department of Cardiology and Organ Systems (COS), Biomedical Research Institute (BIOMED), Faculty of Medicine and Life Sciences, Hasselt University, Diepenbeek, Belgium

[10] Laboratory of Lipid Metabolism and Cancer, Department of Oncology, Leuven Cancer Institute, KU Leuven, Leuven, Belgium

[11] Cellular Communication and Neurodegeneration Research Group, Animal Physiology and Neurobiology Division, Department of Biology, KU Leuven, Leuven, Belgium

[12] Neural Circuit Development and Regeneration Research Group, Animal Physiology and Neurobiology Division, Department of Biology, Leuven Brain Institute, KU Leuven, Leuven, Belgium

[13] imec, Kapeldreef 75, Leuven 3001, Belgium

Introduction

Oligodendrocytes, the myelinating cells of the human central nervous system (CNS), are vital for axonal insulation, efficient action potential conduction, and the overall maintenance of neuronal health. Myelination is a dynamic and lifelong process, which relies on the coordinated interactions between oligodendrocytes and neurons, leading to the synthesis and maintenance of lipid-rich myelin sheaths that are crucial for proper CNS function [1]. Disruption of this process is implicated in a range of demyelinating disorders, such as Multiple Sclerosis (MS), Neuromyelitis Optica, and Leukodystrophies [2, 3]. Recent studies have shown significant species-specific differences in the structure and function of the myelin sheath, particularly between rodents and humans [4, 5]. These differences encompass proteomic [6] and lipidomic composition [7], structural organization (such as variations in myelin thickness and internode length) and the timing of oligodendrocyte maturation [8]. Hence, current rodent models fail to capture the intricate processes of human myelin biology, limiting insights into its role in health and disease. Consequently, there is a critical unmet need for a human myelin model that faithfully replicates the temporal maturation stages of myelin sheath formation – from early loose wrapping around axons to the compact, multilamellar myelin characteristic of mature oligodendrocytes. Such a model would offer transformative insights into myelin formation, its disruption in disease and remyelination strategies upon injury, paving the way towards novel therapeutic strategies to treat demyelinating disorders.

Advances in human pluripotent stem cell (hPSC) and brain organoid technologies have led to the development of self-organizing three-dimensional (3D) models that closely recapitulate the neural cytoarchitecture and transcriptional programs of in vivo human brain development. However, in most current models, axonal myelination typically does not occur until at least 8–12 weeks in culture [9–17] (Table S4). These hPSC-derived organoids are usually initiated from a single pluripotent population that undergoes spontaneous or directed differentiation, thereby mimicking, to some extent, early brain developmental trajectories. Like in vivo development, oligodendrocyte lineage cells appear later in culture and require additional time to mature. In the human brain, the transition from oligodendrocyte precursor cells (OPCs) to mature, myelinating oligodendrocytes begins in late fetal development and continues well into the postnatal period, especially during the first few years of life [18]. As a result, the existing in vitro hPSC models predominantly capture only early-stage neuron-glia interactions, while oligodendrocyte maturation and myelin formation remain largely immature. This immaturity is evidenced by the scarcity of compact, multilamellar myelin sheaths and the presence of immature transcriptional signatures in oligodendrocyte populations [16, 19].

Fig. 1 Generation and characterization of Sigma-iPSC0028 iPSCs derived MyS and NMS). **a** Schematic representation depicting the generation of MyS and NMS by coculturing human pluripotent stem cells (hPSCs) derived pre-differentiated cortical neural (NPCs) and oligodendrocyte precursor cells (OPCs) in hanging drops followed by dynamic culture. **b** Growth of MyS and NMS over 15 weeks of dynamic culture indicated by the quantified diameters of MyS and NMS on the brightfield images. **c** Gene expression analysis by RT-qPCR showing significantly higher transcript levels of oligodendrocyte markers (*MBP*, *SOX10* and *OLIG2*) in week 10 MyS as compared to NMS. **d-f** Confocal microscopic images showing the expression of neuronal (MAP2, NeuN), astrocytic (S100β, GFAP) and oligodendrocyte (MBP, CNP) markers in week 10 NMS and MyS via immunostaining (scale bar = 100 μm and 25 μm for zoomed images). Nuclei were counterstained with Hoechst. **g-i** Quantification based on immunostaining images showing significantly higher percentage of NeuN, GFAP and MBP positive cells in week 10 MyS than NMS. Statistical analyses were performed by two-way ANOVA with Sidak's comparison test (b) or unpaired two tailed *t*-tests (c, g-i). Data shown are mean ± SD. $^{*}p<0.05$, $^{**}p<0.01$, $^{****}p<0.0001$. $N=1$ ($n=8$–32 spheroids, b), $N=3$ ($n=3$–6 spheroids, c), representative immunostaining images for $N=3$ (d-f), $N=3$ ($n=3$–4, each data point represents 3 slices, g-i)

We developed a novel hPSC-derived 3D spheroid model known as Myelin Spheres (MyS), generated by coculturing neural precursor cells (NPCs) with pre-differentiated OPCs to study myelination. As a control, Neuron Monoculture Spheroids (NMS) composed of NPCs alone were also generated. Using a combination of single-nuclei RNA sequencing, lipidomics, electrophysiology and electron microscopy, we demonstrated that MyS supported significantly greater oligodendrocyte maturation and compact myelin formation compared to NMS. These findings demonstrate that incorporating pre-differentiated OPCs accelerates and enhances myelination, offering a more physiologically relevant platform for modeling myelin-related diseases. As a proof-of-concept, MyS was used as a disease modeling platform to study two pathological paradigms: lysolecithin-induced demyelination and Rabies virus infection.

Results

1. Generation and characterization of Neuron Monoculture Spheroids (NMS) and Myelin Spheres (MyS).

We cocultured pre-differentiated cortical neural precursor cells (NPCs) and inducible *SOX10* (i*SOX10*) oligodendrocyte precursor cells (OPCs) using a hanging drop method to generate MyS (Fig. 1a). As control, NMS were generated by culturing only NPCs in hanging drops. Both NMS and MyS were cultured in medium supplemented with growth factors supporting oligodendrocyte differentiation for 6–15 weeks. Throughout the whole culture period, NMS were larger in

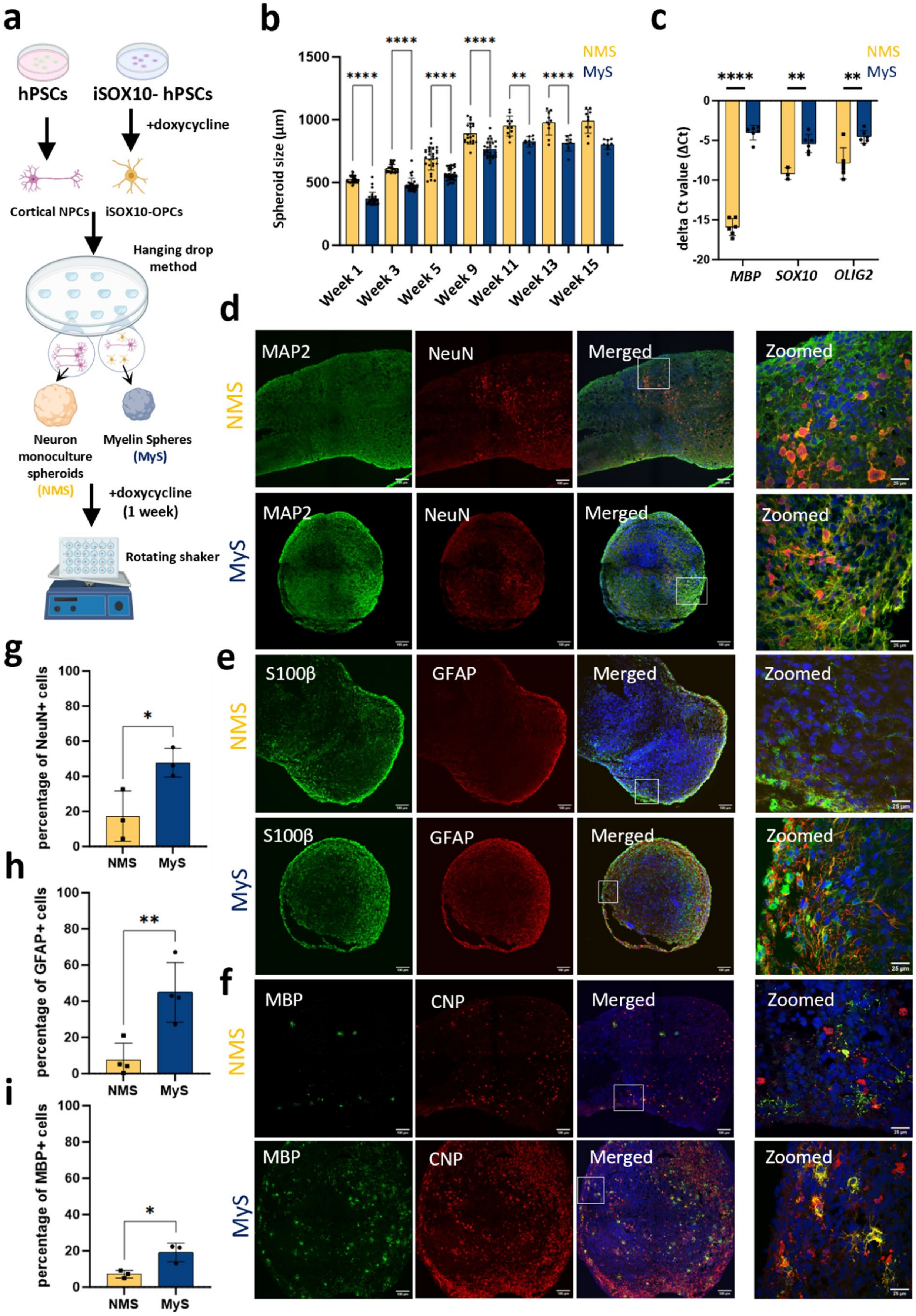
a
hPSCs
iSOX10- hPSCs
+doxycycline
Cortical NPCs
iSOX10-OPCs
Hanging drop method
Neuron monoculture spheroids (NMS)
Myelin Spheres (MyS)
+doxycycline (1 week)
Rotating shaker
b
Spheroid size (µm)
1500
1000
500
0
****
****
****
****
**
****
NMS
MyS
Week 1
Week 3
Week 5
Week 9
Week 11
Week 13
Week 15
c
delta Ct value (ΔCt)
0
-5
-10
-15
-20
****
**
**
NMS
MyS
MBP
SOX10
OLIG2
d
NMS
MyS
MAP2
NeuN
Merged
Zoomed
e
NMS
MyS
S100β
GFAP
Merged
Zoomed
f
NMS
MyS
MBP
CNP
Merged
Zoomed
g
percentage of NeuN+ cells
100
80
60
40
20
0
*
NMS
MyS
h
percentage of GFAP+ cells
100
80
60
40
20
0
**
NMS
MyS
i
percentage of MBP+ cells
100
80
60
40
20
0
*
NMS
MyS

diameter than MyS, likely due to higher initial number of more proliferative NPCs, as compared to MyS (Fig. 1b).

By real-time quantitative polymerase chain reaction (RT-qPCR) we observed that expression of key transcripts for NPCs (*NESTIN*, *SOX2*), maturing neurons (*TUBB3*, *MAP2)* and astroglial (*S100β*, *SOX9*, *AQP4 and ALDH1L1*) in week 10 NMS and MyS were similar (Figure S1 a-b). Immunostaining for neuronal (MAP2, NeuN, CTIP2, SATB2) and astrocytic markers (GFAP, EAAT1, S100β) (Fig. 1d–e, Figure S1c–d) revealed the presence of well-defined neuronal and astroglial populations. Quantification of $NeuN^+$ neurons and $GFAP^+$ astrocytes indicated a higher abundance of mature neurons and astrocyte-lineage cells in MyS compared to NMS (Fig. 1g–h). We also performed RT-qPCR and immunostaining for OPC- and oligodendrocyte-specific markers on week 10 NMS and MyS. RT-qPCR confirmed the presence of higher levels of OPC (*SOX10*, *OLIG2*) and oligodendrocyte (*MBP*) transcripts in MyS compared to NMS (Fig. 1c). Immunostaining revealed that both NMS and MyS contained cells expressing oligodendrocyte specification transcription factors (OLIG2, SOX10) (Figure S1e) and mature oligodendrocyte markers (MBP, CNP) (Fig. 1f). The presence of cells with an OPC or mature oligodendrocyte phenotype in NMS is likely due to the use of oligodendrocyte maturation medium (OMM) containing cytokines that support oligodendrocyte generation and maturation. Nevertheless, a significantly greater percentage of mature oligodendrocytes was present in MyS compared to NMS (Fig. 1i).

2. MyS-derived oligodendrocytes transcriptome closely resemble adult human oligodendrocytes.

To gain deeper insight into the dynamics of cell lineage progression in MyS and NMS, we performed single-nuclei RNAseq (snRNAseq) at both 8-week and 15-week time points. We first assessed the generation of different neural cell populations in both MyS and by combining the 8 and 15 week datasets of both MyS and NMS models. By categorizing cells based on their gene expression profiles using Uniform Manifold Approximation and Projection (UMAP) dimensionality reduction (Fig. 2a), we identified clusters according to established markers for progenitor cells (*TOP2A* and *MKI67*), oligodendrocytes (*MBP* and *PLP1*), OPCs (*PCDH15* and *PDGFRα*), astrocytes (*GFAP* and *AQP4*), and neurons (*RBFOX3*, *BCL11B*, *SLC17A7*, *NEUROD6*, *GAD1* and *GAD2*) (Fig. 2b and Figure S2a-d). Marker gene analysis revealed defining cluster-specific marker sets (Table S2). To further confirm the identity of the cellular clusters, we performed gene ontology (GO) enrichment analysis. This validated the identities of the clusters previously inferred based on marker expression (Fig. 2c and Figure S2e). Notably, the term "Myelination (GO: 0042552)" emerged as the most enriched term in the GO

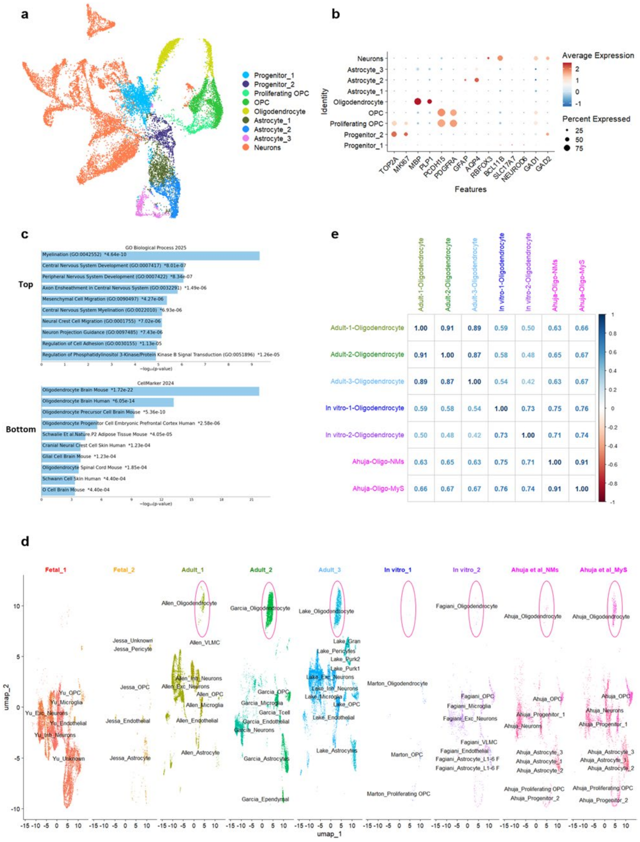

	Adult-1-Oligodendrocyte	Adult-2-Oligodendrocyte	Adult-3-Oligodendrocyte	In vitro-1-Oligodendrocyte	In vitro-2-Oligodendrocyte	Ahuja-Oligo-NMs	Ahuja-Oligo-MyS
Adult-1-Oligodendrocyte	1.00	0.91	0.89	0.59	0.50	0.63	0.66
Adult-2-Oligodendrocyte	0.91	1.00	0.87	0.58	0.48	0.65	0.67
Adult-3-Oligodendrocyte	0.89	0.87	1.00	0.54	0.42	0.63	0.67
In vitro-1-Oligodendrocyte	0.59	0.58	0.54	1.00	0.73	0.75	0.76
In vitro-2-Oligodendrocyte	0.50	0.48	0.42	0.73	1.00	0.71	0.74
Ahuja-Oligo-NMs	0.63	0.65	0.63	0.75	0.71	1.00	0.91
Ahuja-Oligo-MyS	0.66	0.67	0.67	0.76	0.74	0.91	1.00

Fig. 2 Single-nuclei RNA sequencing results unveiled a notable transcriptomic congruence between mature oligodendrocytes and Sigma-iPSC0028 iPSCs derived MyS- or NMS-derived oligodendrocytes. **a** The UMAP embedding of MyS and NMS revealed nine distinctive clusters (progenitor_1, progenitor_2, oligodendrocyte precursor cells (OPC), proliferative OPC, oligodendrocytes, astrocytes_1, astrocytes_2, astrocytes_3, neurons) characterized by specific transcriptomic signatures of different brain cells. **b** Dotplot shows the average expression and percentage of cells expressing markers for progenitor cells, OPCs, oligodendrocytes, astrocytes, and neurons within each cell cluster. **c** Enrichment analysis of the oligodendrocyte cluster highlighted a significant enrichment of the BP-annotated myelination pathway based on the differentially upregulated genes. Additionally, the cells were matched to those of oligoendrocytes in both mouse and human brains, according to the CellMarker 2024 database (https://maayanlab.cloud/Enrichr/). **d** Cells derived from MyS and NMS exhibit transcriptomic profiles more similar to in vivo brain cells than other in vitro models (the oligodendrocytes are highlighted within the pink ellipse), shown by the UMAP representation of integrated sn/scRNA-seq datasets, which include MyS and NMS samples, in vivo adult (Adult_1: Bakken et al.[79, 80]; Adult_2: Garcia et al. [39]; Adult_3: Lake et al.[38]) and developing brain cells (Fetal_1: Yu et al.[35]; Fetal_2: Jessa et al. [36]), and two in vitro brain models (In vitro_1: Marton et al. [19], In vitro_2: Fagiani et al.[16]). **e** Oligodendrocytes present in MyS and NMS are more similar to adult oligodendrocytes from three different in vivo datasets [37–39] compared to oligodendrocytes developed in two in vitro models [16, 19] by correlation analysis (shown in pink rectangle). BP: biological process, UMAP: Uniform Manifold Approximation and Projection

biological processes analysis for the cluster identified as oligodendrocytes (Fig. 2c, top). Additionally, the gene expression profile in this cluster significantly matched that of oligodendrocytes in both mouse and human brains, according to the CellMarker 2024 datasets (Fig. 2c, bottom).

Subsequently, we assessed if coculturing iSOX10 oligodednrocyte progenitors with NPCs (MyS) would yield earlier/more mature oligodendrocytes compared to cortical precursor only cultures (NMS) by evaluated the DEGs in the oligodendrocyte and OPC clusters between NMS and MyS at weeks 8 and 15 (using an adjusted p-value $<$ 0.05 and a log2 fold-change $>$ 1) (Table S3). We observed stronger transcriptional differences between NMS and MyS at week 8 compared to week 15. At week 8, 33 genes were upregulated in NMS-derived oligodendrocytes (e.g., *ADAM23*, involved in juxtaparanodal organization [20], and *GAB1*, a PDGF effector regulating OPC differentiation [21]), while only two were upregulated in MyS-derived oligodendrocytes (*TMSB4X*, which promotes cytoskeletal stability and myelin protein phosphorylation [22, 23], and *MT-ND3*, a mitochondrial gene linked to increased metabolic demand during maturation [24–26]). In OPCs, 118 and 88 genes were upregulated in NMS and MyS respectively. NMS showed enrichment of early-stage transcription factors (*SOX4*, *SOX9*, and *PARP1)*, known to maintain progenitor identity or inhibit terminal differentiation [27–29]. By contrast, MyS-derived OPCs showed higher expression of genes promoting myelin membrane synthesis and maturation (*PLPP4*, *UGT8*, *LRRK2*, and *TMEFF2)* [30–33]. By week 15, transcriptional differences had diminished, with only three upregulated genes in NMS-derived oligodendrocytes and none in MyS. However, MyS-derived OPCs continued to show a maturation bias, with upregulation of genes important for lipid processing and cholesterol homeostasis (*LRP1B)* [34]. Together, these findings confirm that MyS cultures promote a more advanced oligodendrocyte maturation compared to NMS.

Next, we assessed the transcriptomic similarity of cellular populations, including the oligodendrocytes, developed in our MyS and NMS brain models with fetal and adult in vivo brain tissues as well as with in vitro brain models. To achieve this, we performed a comprehensive integrated analysis, incorporating references from two fetal [35, 36] and three adult [37–39] sn/scRNAseq brains datasets, as well as two in vitro hPSC-derived brain datasets [16, 19] (Fig. 2d). This indicates a strong transcriptional similarity across the datasets, suggesting that the cellular populations in our models exhibit transcriptional profiles closely resembling those of adult human brain cells (Figure S3a). Notably, MyS cultures contained a substantially higher proportion of oligodendrocytes (12.2% vs. 1.45% week 8 and 7.52% vs. 1.84% week 15) and astrocytes (14.03% vs. 11.02% week 8 and 34.22% vs. 21.00% week 15) compared to NMS. Next, we performed a Spearman correlation analysis. We also compared oligodendrocytes across datasets. Using two complementary approaches, we compared our models with publicly available in vitro and in vivo datasets. First, NMS- and MyS-derived oligodendrocytes from weeks 8 and 15 were combined into a single object and compared with reference datasets. This analysis revealed that MyS-derived oligodendrocytes exhibited higher correlation with adult human brain samples (0.66–0.67 [37–39]) than oligodendrocytes from the in vitro models of Marton et al. (0.54–0.59) [19] and Fagiani et al. (0.42–0.50) [16] (Fig. 2e). These findings were further supported by comparative pseudobulk analyses visualized using scatter plots (Figure S4a–d). In a second approach, we segmented our dataset into four individual groups (NMS week 8, MyS week 8, NMS week 15, and MyS week 15) and repeated the correlation analysis. This stratified analysis showed that oligodendrocytes from both NMS (0.61–0.62) and MyS (0.65–0.66) at week 8 were already more transcriptionally similar to adult human oligodendrocytes [37–39] than those generated in other in vitro models (Marton et al.- 0.54–0.59) [19], particularly the Fagiani in vitro model (0.42–0.50) [16], despite the use of a similar *SOX10* overexpression strategy (Figure S3b–c). We next performed Slingshot trajectory analysis on the integrated dataset to position oligodendrocytes derived from MyS and NMS within a developmental context. Using a supervised approach, we designated the youngest (9–12 weeks) fetal OPCs as the starting point [35]. This revealed three distinct lineages (Fig. 3a). In the first lineage, MyS-derived oligodendrocytes appeared downstream of fetal OPCs and oligodendrocytes from the Marton et al. study [19] but preceding mature adult oligodendrocytes [37–39], suggesting a continuous trajectory toward maturation. The second and third trajectories did not extend to any adult oligodendrocyte populations. In the second trajectory, NMS and MyS oligodendrocytes were located very close together but downstream of oligodendrocytes from Marton et al.[19], and fetal OPCs [35, 36]. The third trajectory included all three in vitro created oligodendrocytes, with MyS-derived oligodendrocytes downstream of fetal OPCs. Collectively, these findings indicate that MyS-oligodendrocytes exhibit greater maturation compared to fetal OPCs and cells from other in vitro models.

To further explore the temporal dynamics of oligodendrocyte development, we performed RNA velocity analysis on week 8 and 15 MyS-derived progenitor, OPC, and oligodendrocyte clusters. The analysis conducted on pooled cells at 8 and 15 weeks MyS, revealed two developmental routes – one progressing directly from progenitors to oligodendrocytes, and another transitioning via OPCs (Fig. 3b). Dynamic gene expression profiling revealed distinct gene

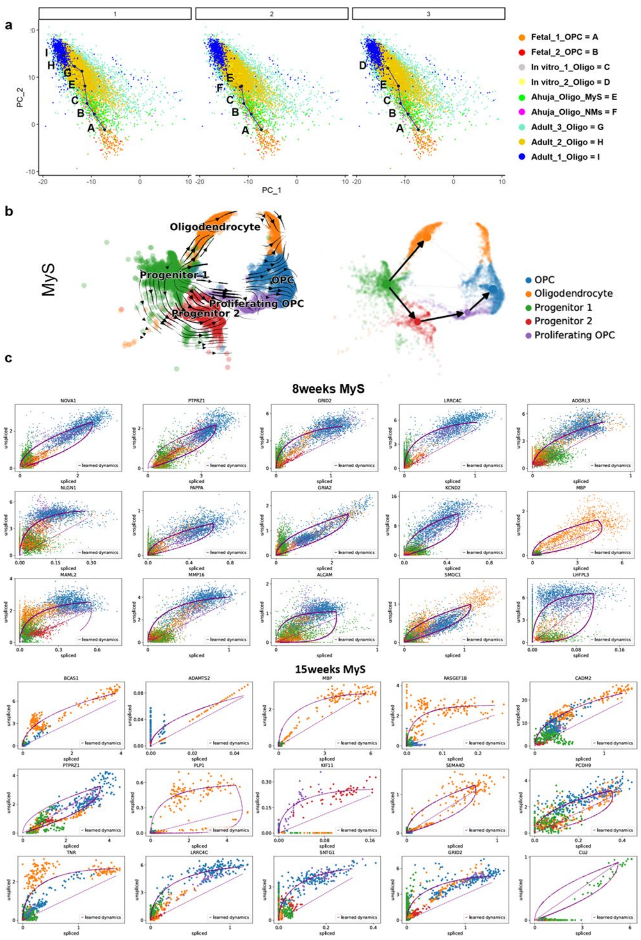

Fig. 3 Enhanced maturation of oligodendrocytes in Sigma-iPSC0028 iPSCs derived MyS compared to NMS, with significant progress observed at 15 weeks. **a** Slingshot analysis of integrated sn/scRNAseq datasets identified three distinct lineages. The first lineage included mature oligodendrocytes, with MyS-derived oligodendrocytes leading the developing OPCs from fetal datasets [35, 36] and oligodendrocytes from the in vitro model in Marton et al.'s [7] study and followed by mature oligodendrocytes [37–39]. The second and third lineages consisted of developing OPCs and oligodendrocytes from in vitro brain models. Notably, in the second lineage, MyS-derived oligodendrocytes preceding NMS-derived oligodendrocytes. **b** Left: Velocity projection onto the UMAP embedding based on the dynamical model revealed two developmental trajectories starting from progenitor cells either directly to oligodendrocytes or via OPCs in MyS. Right: The PAGA velocity graph, overlaid on the UMAP embedding, provides a visualization of potential transitions between cell types. In this representation, nodes denote cell groups, while edge weights measure the connectivity between these groups. **c** Genes from MyS-derived cells at 8 and 15 weeks that exhibit significant dynamic behavior, positioning them as potential key drivers of the primary processes within certain cell populations. These genes were systematically identified through their characterization by high likelihoods in the dynamic model [40]

sets at weeks 8 and 15, likely acting as key regulators of oligodendroglial maturation within defined cellular states [40] (Fig. 3c). Notably, clustering of OPCs and oligodendrocytes in week 15 MyS became more prominent along the developmental trajectory compared to those in week 8 MyS, indicating progressive maturation of the oligodendroglial lineage in MyS over time (Figure S5a–b, Table S4 and 5). At week 8, we found highly dynamic genes involved in early lineage commitment, synaptic signaling, and initial onset of myelin-related gene expression (*PTPRZ1*, *GRIA2*, and *KCND2)* [19, 41, 42]. Notably, *MBP* expression emerged at this stage, marking the onset of myelin gene activation. By week 15, several highly dynamic genes associated with MyS-derived oligodendrocytes were identified, exhibiting a transcriptional profile indicative of advanced maturation (*BCAS1*, *PLP1*, and *MBP*), which are crucial for active myelination and myelin compaction [43–45]. The continued presence of *PTPRZ1* in OPCs and *ADAMTS2* in oligodendrocytes further suggests roles in structural maintenance of mature oligodendrocytes [46]. These results support a temporal progression in MyS cultures from early OPCs toward myelinating oligodendrocytes.

3. Temporal development of myelin sheaths in MyS.

We further analyzed oligodendrocyte maturation in MyS versus NMS by immunocytochemistry and transmission electron microscopy (TEM). Immunostaining of MyS demonstrated that neurons (TUBB3$^+$), astrocytes (GFAP$^+$), and elaborately branched oligodendrocytes (MBP$^+$) were positioned in close proximity, with interwoven processes and complex morphologies suggestive of active cell-cell interactions (Fig. 4a). This spatial arrangement was further supported by 3D rendering of the immunofluorescence images, which highlighted the intricate architecture and contact points between these cell types (Fig. 4b). By contrast, the number of MBP$^+$ oligodendrocytes in NMS was markedly lower, resulting in very few observable neuron-oligodendrocyte interaction sites (data not shown). TEM revealed that myelinated axons were already present in MyS at six weeks of culture (Fig. 4c-d, Video S1 at week 10). To evaluate myelin maturation over time, we quantified multiple structural parameters on loose, mid-compact and compact structures in 10- and 15-week-old MyS, including G-ratio, axon radius, number and thickness of myelin lamellae per axon, and the percentage of different myelin types. In week 10 and 15 MyS, the G-ratio was lowest in loosely organized myelin structures (~0.5), compared to mid-compact (~0.72) and compact (~0.66) myelin, indicating increased axonal wrapping with advancing myelin compaction (Fig. 4e). Compact myelin sheaths containing more myelin lamellae with lesser thickness, were mainly found around lower-diameter axons. By contrast, mid-compact myelin structures having fewer but thicker myelin lamellae were found around bigger axons, which was not different in week 10 or week 15 MyS (Fig. 4f-g). The myelin lamellar thickness was the highest in

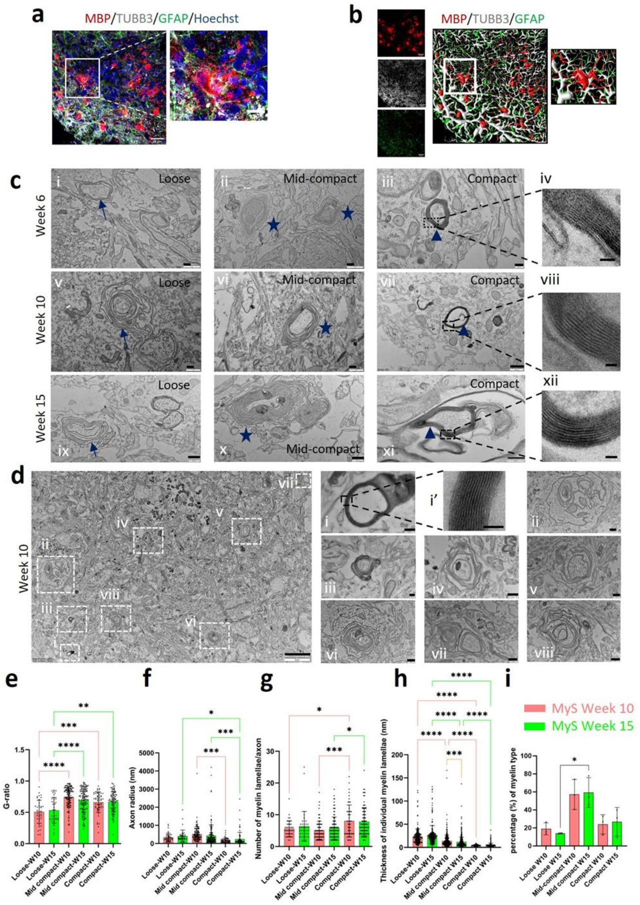

Fig. 4 Oligodendrocyte maturation leading to formation of myelin sheaths in Sigma-iPSC0028 derived MyS. **a** Representative confocal image showing immunostained MBP$^+$ oligodendrocyte processes interacting with TUBB3$^+$ neurons and GFAP$^+$ astrocytes in MyS at week 10. Nuclei were counterstained with Hoechst. **b** 3D rendering of confocal reconstructed image indicating TUBB3$^+$ neurons surrounded by MBP$^+$ oligodendrocyte and GFAP$^+$ astrocytes processes in MyS at week 10. **c** Representative TEM images showing formation of different subtypes of myelin sheaths (loose (arrow) i, v, ix), mid-compact ((star) ii, vi, x) and compact ((triangle) iii, iv, vii, viii, xi, xii) in MyS at week 6,10 and 15 (scale bar = 500 nm: i, ii, v, vi, vii, ix, x; 200 nm: iii, xi; 45 nm: iv, xii; 25 nm: viii). **d** Representative TEM images showing distribution and types of myelin sheaths in MyS at week 10 (scale bar = 5 µm, 200 nm = i, iii; 45 nm = i'; 500 nm = ii, iv-viii). **e-i** Quantification of myelin sheath parameters: G-ratio, axon radius, number of myelin lamellae/axon, thickness of myelin lamellae and percentage of myelin type in MyS at week 10 and 15. Statistical analyses were performed by Two-way ANOVA with Sidak's comparison test (**e-i**). Data shown are mean ± SD. (a-d) Representative TEM images from $N=3$ replicates, (e-i) $N=3$ (at least 200 axons ($n>200$) for all parameters) for myelin quantification. *$p<0.05$, **$p<0.01$, ***$p<0.001$, ****p0.0001

loose myelinated axons compared to mid-compact and compact myelinated axons. However, myelin lamellar thickness was lower in week 15, compared to week 10 mid-compact myelinated axons, indicating myelin compaction over time in MyS (Fig. 4h). Further, the percentage of mid-compact myelinated axons was higher than loose myelinated neurons in week 15 compared to week 10 MyS (Fig. 4i). Consistent with the presence of a small number of MBP$^+$ oligodendrocytes in NMS (Fig. 1f), we observed limited myelinated axons in week 10 NMS (Figure S6a), supporting more robust and organized myelin formation in MyS.

We also created NMS and MyS from human H9-ESC line derived NPCs and human i*SOX10*-H9-ESC OPCs to study stem cell line independent myelination. This revealed a similar pattern of oligodendrocyte presence using immunostaining for neurons (TUBB3$^+$) and oligodendrocytes (MBP$^+$) (Figure S6b- week 10), as well as myelination by TEM (Figure S6c- week 6, 10 and 13 and Video S2- week 10) in H9-ESC derived MyS and NMS. Again, only few myelinated axons were observed in H9-ESC derived NMS (data not shown).

4. Lipidomic profile supports myelin maturation over time in MyS.

Lipids, especially cholesterol, are essential for CNS myelin sheaths, providing structural integrity, insulation, and facilitating rapid nerve impulse conduction. To demonstrate greater abundance of mature oligodendrocytes in MyS compared to NMS, a detailed lipidomic analysis was performed. The technical replicates of both NMS and MyS at weeks 8 and 15 clustered together in principal component analysis indicating technical reproducibility (Fig. 5a), while heatmap visualization revealed substantial differences in lipid composition across the four groups (Figure S7a). We observed 17 lipid subclasses from which the relative amounts of phosphatidylcholine (PC) and phosphatidylethanolamine (PE) were the most represented in both NMS and MyS as reported in in vivo studies [47] (Fig. 5b).

To focus on changes in lipid fingerprint related to oligodendrocyte maturation and myelin sheath formation in NMS and MyS, we focused on five lipid classes: glycerolipids (triglycerides (TG) and diglycerides (DG); Figure S7b-c), phospholipids (PL) (e.g. phosphatidylcholine (PC), lysophosphatidylcholine (LPC), phosphatidylethanolamine (PE), lysophosphatidylethanolamine (LPE), phosphatidylglycerol (PG), and phosphatidylinositol (PI); Figure S7d-i), sphingolipids (including sphingomyelin (SM), ceramides, hexosylceramides, hexosyl-2-ceramides; Figure S7j-m), esther linked phospholipids (Figure S7n-q), and cholesteryl esters (CE). Glycerolipid levels declined over time in both models but remained moderately higher in MyS compared to NMs at both 8 and 15 weeks (Fig. 5c). A similar trend was observed for phospholipids, which showed a slight decline over time but remained higher in MyS compared to NMS at both time points (Fig. 5d). These patterns suggest a possible metabolic shift toward higher myelin lipid synthesis and incorporation into myelin membranes in MyS

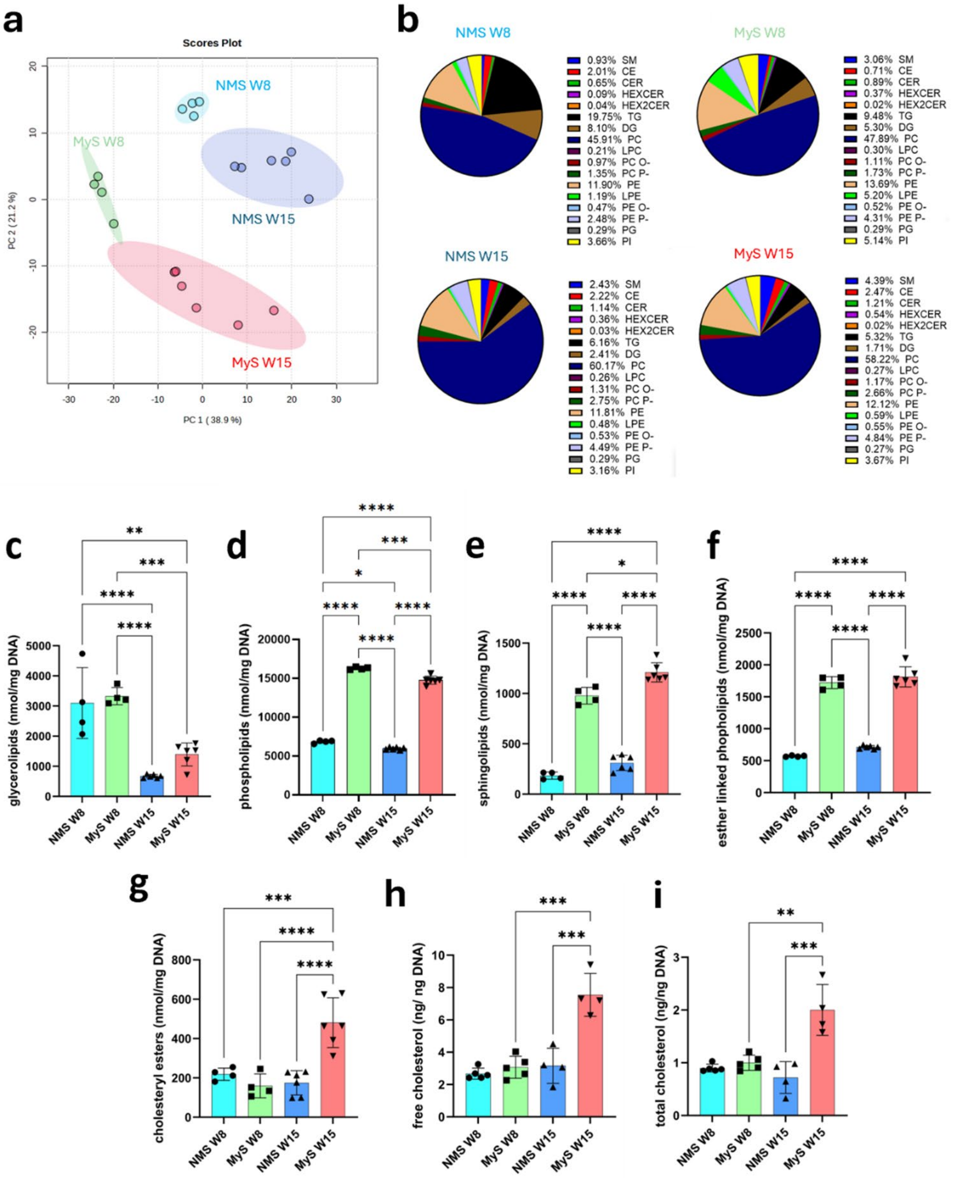

Fig. 5 Temporal increase in myelin lipids in Sigma-iPSC0028 iPSCs derived MyS suggesting maturation of myelin sheaths. **a** PCA analysis showing distinctive clustering of MyS and NMS samples at week 8 and 15. **b** Pie charts indicating the different types of lipid species identified by lipidome analyses in NMS and MyS at week 8 and 15. **c-g** Comparison of absolute amount of different major lipid classes identified in NMS and MyS at week 8 and 15 by lipidome analysis: glycerolipids, phospholipids, sphingolipids, esther linked phospholipids, and cholesteryl esters. **h-i** Cholesterol (free and total) detection assay confirming the highest cholesterol amount in MyS at week 15 as compared to other conditions. Statistical analyses were performed by Two-way ANOVA with Sidak's comparison test (**c-i**). Data shown are mean ± SD, $n = 4–6$. $*p<0.05$, $**p<0.01$, $***p<0.001$, $****p<0.0001$. SM: Sphingomyelin, CE: Cholesteryl Esters, CER: Ceramides, HEXCER: Hexosylceramides, HEX2CER: Hexosyl-2-Ceramides, TG: Triglyceride, DG: Diglyceride, PC: Phosphatidylcholines, LPC: Lyso-Phosphatidylcholines, PC O-: Ether-linked Phosphatidylcholines, PC-P-: Plasmalogen Phosphatidylcholines, PE: Phosphatidylethanolamines, LPE: Lyso-Phosphatidylethanolamines, PE O-: Ether-linked Phosphatidylethanolamines, PE P-: Plasmalogen Phosphatidylethanolamines, PG: Phosphatidylglycerols, PI: Phosphatidylinositol

compared to NMS. Sphingolipids remained stable in NMS but increased slightly in MyS over time, with overall levels higher in MyS across both weeks (Fig. 5e). Esther linked phospholipids showed no significant temporal change in either model but were consistently higher in MyS than NMS (Fig. 5f). Cholesteryl esters were notably higher in week 15 MyS compared to both week 8 MyS and NMS, indicating increased lipid storage or altered cholesterol metabolism at this stage (Fig. 5g). In line with these class-level changes, lipid ratio analysis indicates both temporal myelin maturation and partial myelin enrichment, with SM/PC values increasing over time and remaining higher in MyS than NMS, while consistently low CE/PL ratios across conditions reflect limited cholesterol esterification typical of developing, rather than fully mature myelin [48–50] (Figure S7r-s). Importantly, given the essential role of cholesterol in myelin sheath stabilization and compaction [51, 52], we further measured cholesterol levels using a fluorometric assay. Both free and total cholesterol levels were significantly elevated in week 15 MyS compared to all other groups (Fig. 5h–i), suggesting progressive metabolically active myelination over time in MyS relative to NMS.

5. MyS are functionally mature compared to NMS.

To assess if myelinating oligodendrocytes influence neuronal activity, we employed high density-multielectrode array (HD-MEA) technology. Week 8–10 MyS and NMS were sectioned and cultured with the sliced surface positioned on HD-MEA plates (Figure S8a). In MyS, spontaneous spiking activity was detected as early as week 4 after plating the MyS slices. Based on the activity maps of MyS slices plated at 1–2 slices per well (Figure S8b), we applied a threshold of ≥150 electrodes with a firing rate > 1 Hz to define activity, identifying 23 active and 10 non-active slices. Detailed analysis of neuronal activity from week 4 to 8 revealed unchanged spike amplitude, along with a significant increase in firing rate and number of active electrodes, as well as a shorter mean interspike interval, indicating enhanced network excitability and maturation (Figure S8c-f). While burst rate showed a non-significant upward trend, the accompanying significant increase in interburst interval further supports progressive network engagement over time (Figure S8g-h). To address variability in network behavior over time, we applied an additional cutoff of a ≥ 30% increase in overall spiking activity between weeks 4 and 8 to classify the slices by activity trend. Based on this threshold, number of active electrodes and firing rate of eight slices (34.8%) maintained activity levels (Figure S8i), three slice (13%) showed a decreasing trend (Figure S8j), 12 out of 23 slices (52.2%) exhibited an increasing trend from week 4 (Figure S8k), also evident in the raster plot at week 4 and 7 (Figure S8l). Conversely, no significant spiking and bursting activity was detected in the NM slice cultures over the 8 weeks of electrophysiology recording (data not shown).

6. MyS to model CNS disorders.

We next assessed if the MyS model could be used to study central nervous system (CNS) diseases. As proof of concept for studying oligodendrocyte injury, we treated week 10 MyS with toxic phospholipid lysolecithin for 15 h, which has been demonstrated to cause demyelination in ex vivo explant cultures [53] and an in vitro myelination model [19]. Week 10 MyS treated with lysolecithin seemed to disintegrate as cells were shed from the spheres (Figure S9a). Immunostaining demonstrated that lysolecithin-treated samples contained less MBP$^+$ oligodendrocytes than untreated control MyS (Figure S9b-c). Consistently, TEM demonstrated that lysolecithin-treated MyS contained broken myelin sheaths (Figure S9d).

We also investigated if the MyS model could be used to study CNS infections, specifically if the model supports Rabies virus (RABV) infection and replication. Week 10 MyS were infected with two different RABV strains, i.e. mCherry-SAD-B19 and CVS-11 (Fig. 6a). RT-qPCR showed a temporal increase in RABV viral RNA in the supernatant of MyS infected with either mCherry-SAD-B19 or CVS-11, reflecting successful viral replication (Fig. 6b). Immunofluorescence microscopy indicated clear viral infection for both virus strains, as shown by the expressed mCherry in mCherry-SAD-B19 infected cultures and by immunostaining for RABV Nucleoprotein in CVS-11 infected cultures. Virus replication was observed in all cultures independent of the virus inoculum (30, 100 or 300 $TCID_{50}$ per spheroid) (Fig. 6c-d). Quantification of the fluorescence signals revealed significant amounts of infected cells for cultures infected with the mCherry-SAD-B19 and CVS-11 strains (Fig. 6e). We also performed TEM to better evaluate the pathological features of RABV infection [54, 55]. We demonstrated the presence of bullet-shaped viral particles (Fig. 6f), mitochondria with disintegrated cristae (Fig. 6g) [56], and degenerated cellular debris (Fig. 6h). In addition, demyelinated neurons were observed, suggesting disruption of neuron-glia interactions either due to degeneration of neurons, glial cells or both (Fig. 6i). We found disrupted neuronal morphology upon infection with CVS-11 but not with mCherry-SAD-B19, correlating with the higher pathogenicity of the CVS-11 RABV strain as compared with the attenuated SAD-B19 vaccine strain, as also shown in mice [57] (Figure S11a). As MyS contain not only neurons, but also astrocytes and oligodendrocytes, we explored if the model would allow the study of RABV cellular tropism. The mCherry-expression for the mCherry-SAD-B19 strain was primarily found in neurons (NeuN$^+$) and oligodendrocyte precursors (OLIG2$^+$) but not in mature oligodendrocytes (MBP$^+$) (Figure S11b). For the CVS-11 RABV strain, we observed colocalization of immunostaining for the viral N-protein with neurons (NeuN$^+$), OPCs (OLIG2$^+$) and oligodendrocytes (MBP$^+$) (Figure S11c). Interestingly neither CVS-11 nor SAD-B19 appeared to colocalize with astrocyte markers (SOX9$^+$/GFAP$^+$). More extensive studies are required to quantify strain-dependent RABV infection.

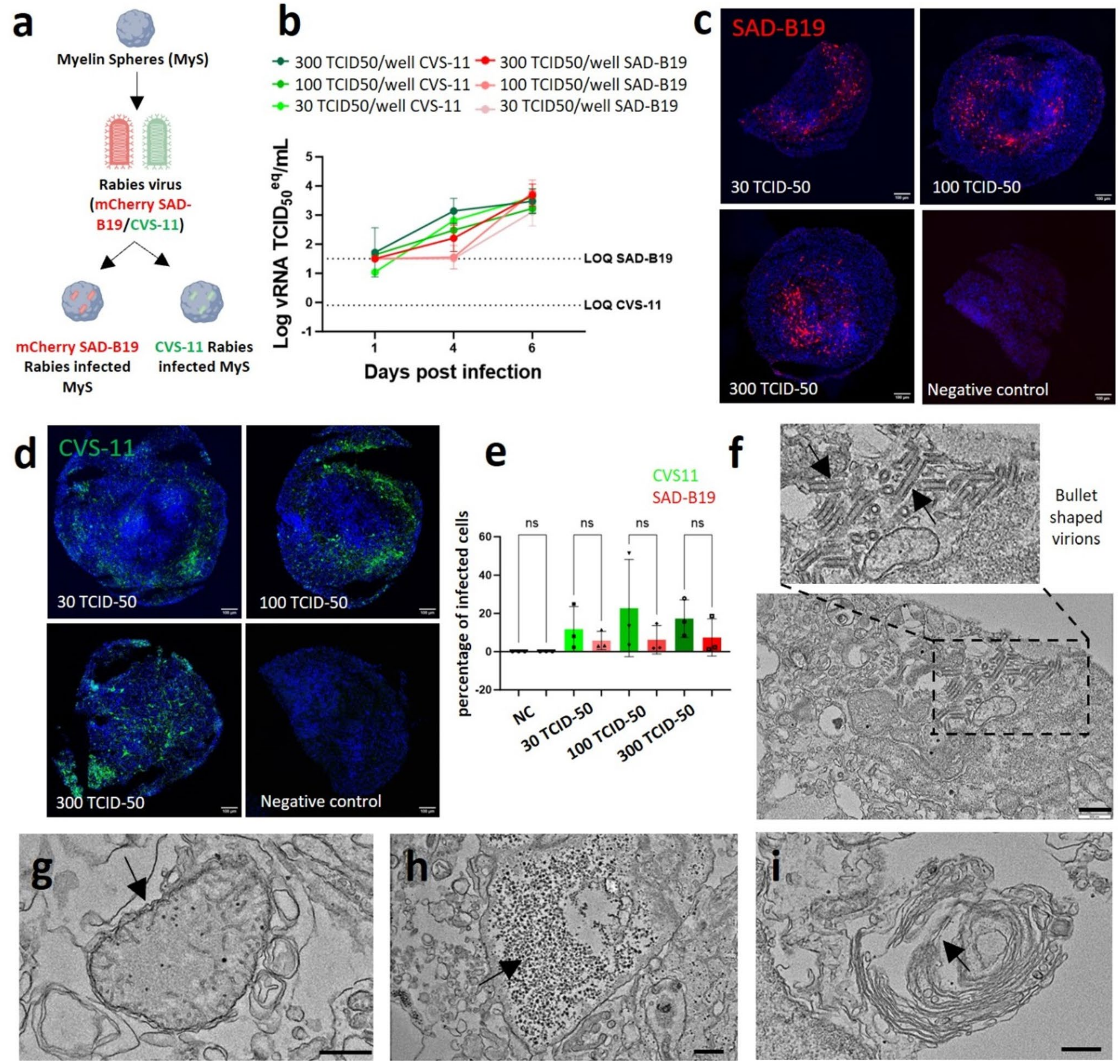

Fig. 6 Rabies infection pathology was recapitulated in vitro using Sigma-iPSC0028 iPSCs derived MyS. **a** Schematic representation of Rabies virus strains (mCherry-SAD-B19 and CVS-11) infection in week 10 MyS. **b** RT-qPCR showing increasing amount of viral RNA by days post infection for both mCherry-SADB19 and CVS11 infection in the supernatant of infected week 10 MyS. Viral RNA was quantified relative to a standard curve of known amounts of viral infectious units (TCID$_{50}$ equivalents of viral RNA (TCID$_{50}$^{eq})). LOQ = Limit of Quantification. **c-d** Fluorescent imaging of mCherry-SAD-B19 and immunostained CVS-11 at three viral concentrations (30, 100 and 300 TCID-50) in week 10 MyS at 5 days post infection (scale bar = 100 µm). **e** Quantification of fluorescence intensity of mCherry-SAD-B19 and CVS-11 in week 10 MyS at 5 days post infection with different viral concentrations. **f-i** Transmission electron micrographs showing several hallmarks of Rabies virus infection like bullet shaped virions (arrow, f), swollen mitochondria with disintegrated cristae (arrow, **g**), cell debris accumulation (arrow, h), axon demyelination (arrow, i). Scale bar = 500 nm. Statistical analyses were performed by Two-way ANOVA with Sidak's comparison test (**e**). Data shown are mean ± SD. *N* = 1, *n* = 3–7 (**b**), representative images and quantification from *N* = 3–4 (c, d, f-i), *N* = 3 (*n* = 3, each data point represents 3 slices e). ns = statistically not significant

Discussion

In this study, we developed hPSC-derived MyS by coculturing cortical NPCs with pre-differentiated i*SOX10*-OPCs to promote neuron-oligodendrocyte interactions and enhance in vitro myelination. Compared to NMS, MyS showed earlier and more robust myelination, with more oligodendrocytes appearing as early as six weeks. Over time, oligodendrocytes in MyS generated increasingly compact and multilamellar myelin sheaths and enhanced neuronal spiking activities, as confirmed by combined ultrastructural, lipidomic and electrophysiology evidence. Consistently, the transcriptomic profile of MyS-derived oligodendrocytes is more similar to adult human brain-derived oligodendrocytes than those produced in other in vitro models [16, 19]. Although MBP$^+$ oligodendrocytes were also present in NMS, likely due to spontaneous differentiation in the presence of endogenous oligodendrocyte-specific growth factors as also reported in other studies [16, 19], their number was substantially lower. Notably, MyS also contained significantly more GFAP$^+$ astrocytes and NeuN$^+$ neurons compared to NMS. This suggests that inclusion of OPCs in MyS may influence the differentiation and maturation of other neural cell types, including astroglia and neurons. However, future studies will be required to further elucidate the mechanisms by which oligodendroglia might promote astroglial and neuronal differentiation, as well as to characterize the differences between MyS- and NM-derived astrocytes and neurons in greater detail.

SnRNAseq on MyS and NMS at week 8 and 15 confirmed the significantly greater percentage of oligodendrocytes (and astrocytes) in MyS. Evaluation of DEGs in OPCs and oligodendrocyte clusters at 8 and 15 weeks, as well as evaluation of highly transcribed genes from RNA velocity studies not only demonstrated much faster oligodendroglial cell development and maturation in MyS than NMS, but also a very clear temporal maturation pattern of MyS-derived oligodendroglial cells. We compared the maturation level of oligodendrocytes generated in MyS (and NMS) with those from other hPSC-based models [16, 19] and with oligodendrocytes from publicly available human brain datasets spanning fetal to adult stages [35–39]. MyS-derived oligodendrocytes showed a stronger correlation with adult brain oligodendrocytes across three snRNAseq datasets (correlation: 0.67–0.70), compared to those from the organoid-based model by Marton et al. [19], which exhibited spontaneous myelination at DIV 100 (correlation: 0.58), and the Fagiani et al.8 model at DIV28-105, which used *SOX10* overexpression in NPCs [16] (correlation: 0.47–0.49). The greater transcriptional maturity of MyS-derived oligodendrocytes, compared to those from NMS and other hPSC-derived models, is further supported by Slingshot analysis of the integrated sn/scRNA-Seq datasets. These analyses support the conclusion that oligodendrocytes generated in MyS cultures exhibit transcriptional profiles more closely resembling adult brain oligodendrocytes compared to those derived from other published hPSC-based models and the current NMS. Notably, the correlation indices between MyS-derived oligodendrocytes and oligodendrocytes generated in the other two PSC-derived in vitro models (> 0.7) were relatively high, suggesting a shared in vitro phenotype. Further, MyS-derived oligodendrocytes also include cells resembling fetal OPCs, as seen in trajectories 2 and 3 – a pattern also observed in oligodendrocytes from Fagiani et al. [16] and Marton et al. [19]. The reasons for the higher degree of transcriptional maturity of MyS-derived oligodendrocytes are likely multiple. Although both the Fagiani et al. [16] and MyS models employ *SOX10* overexpression to induce the oligodendrocyte lineage, differences in experimental design likely contribute to the observed maturation differences. In Fagiani et al. [16], transcriptomic analyses were performed 8 weeks after *SOX10* transduction in NPCs, whereas in the MyS model, analyses were conducted at weeks 8 and 15 following coculture of NPCs with 24-day-old iSOX10-OPCs, allowing for a longer and more developmentally relevant maturation period. To enable a direct comparison, we reanalyzed our data by separating the datasets into four groups (NMS week 8, MyS week 8, NMS week 15, and MyS week 15; Figure S3a–c). This analysis revealed that oligodendrocytes from both NMS and MyS at week 8 are more transcriptionally similar to adult human oligodendrocytes than those generated in the Fagiani in vitro model. On the other hand, MyS and Marton et al. [19]cultures had similar overall durations (80–129 vs. 100 days), yet only MyS included directed *SOX10* induction, underscoring the role of transcriptional programming and OPC pre-commitment in promoting more mature, adult-like oligodendrocyte development in MyS.

To further assess the development of mature oligodendrocytes, we performed detailed lipidomic analysis and cholesterol quantification in NMS and MyS cultures – an approach that, to our knowledge has not been previously applied to human in vitro myelination models. Consistent with the snRNAseq data, we detected significantly greater levels of lipids associated with myelin maturation and compaction in MyS. Notably, sphingolipids, essential for myelin sheath formation and stabilization [58], increased over time in MyS, while glycerolipids and phospholipids decreased, suggesting a metabolic shift toward specialized myelin lipid production. Furthermore, the observed increase in cholesteryl esters, as well as free and total cholesterol, in week 15 MyS relative to both week 8 MyS and week 8 or 15 NMS provides strong evidence for progressive myelin membrane compaction. Importantly, analysis of key lipid ratios, including SM/PC and CE/PL, remained within ranges characteristic of developing rather than fully mature myelin, indicating that while MyS exhibit progressive myelin maturation and compaction, they do not yet reach an adult myelin lipid profile. These lipidomic findings are in line with the RNA velocity analysis, revealing greater activity of genes involved in myelin compaction and terminal oligodendrocyte maturation at week 15.

Presence and maturation of myelin in MyS was corroborated by TEM analysis. The G-ratio of myelinated axons in MyS (0.5–0.75) was in the range seen in the adult human cortex (0.5–0.6), suggesting that myelination in MyS recapitulates to a certain extent the in vivo developmental process [59, 60]. Nevertheless, the number of myelin lamellae per axon (i.e. 5–8 lamellae) in MyS was still more fetal-like, as myelinated axons in adult human brain cortex typically contain 10–50 myelin lamellae [61].

The measured neuronal activities in MyS, but not in NMS, by HD-MEAs suggest the functionality of the myelinating oligodendrocytes in MyS. However, as we did not perform extensive immunostaining controls for recorded NM slices, we cannot exclude that neurons from NMS are more fragile and may be more prone to damage during medium changes. It should also be noted that only ± 75% of MyS slices were functionally active, and that an increase in temporal electrophysiological activity was only seen in ± 50% of these slices. This variability may stem from biological differences in neuron-glia interactions across spheroids or from technical limitations, such as inconsistent attachment of MyS slices to HD-MEAs. In the future, this could be assessed by immunostainings for neurons, astrocytes and oligodendrocytes; however this approach is difficult in longitudinal studies unless lineage-specific fluorochromes are introduce in hPSCs. In addition, the random 3D alignment of axons in MyS makes it nearly impossible to evaluate features such as the effect of myelination on conduction velocity. This problem could be resolved by culturing MyS in scaffolds structures or microfluidics, which would align the axons in one direction. Combined with HD-MEAs, this would enable stimulating soma and detecting the electrical signals at the level of axons.

Lastly, to explore the applicability of the MyS model for studying neurological diseases, we established two pathological paradigms – (1) lysolecithin-induced demyelination and (2) RABV infection. Marton et al. [19] demonstrated that lysolecithin decreases the percentage of SOX10 positive oligodendroglia in their hPSC-derived cultures, in line with our data on structural deformation of myelin sheaths using TEM. Importantly, extending the culture of MyS following exposure to low concentrations of demyelinating agents such as lysolecithin, combined with pharmacological interventions, would provide a valuable platform to assess remyelination dynamics and evaluate candidate remyelinating therapies in a human-relevant system. Rabies is a fatal neurotropic disease with a > 99.9% mortality rate once neurological symptoms appear. We demonstrated successful RABV infection of MyS via immunofluorescence and TEM, and observed some degree of strain-dependent neurotropism [62]. Notably, infection of astrocytes by the CVS-11 strain has been shown to depend on the route of administration in mouse models, underscoring how viral tropism is shaped by experimental conditions [63]. Furthermore, reports of RABV localization in Schwann cells [64] suggest a capacity to target myelinating cells, although earlier studies offer conflicting evidence on this phenomenon [65, 66]. While precise quantification of cell type-specific infection in the MyS model was difficult, due to tight cell-cell contacts, immunostaining did not demonstrate infection of astrocytes by the pathogenic CVS-11 or the attenuated SAD-B19 strain. In addition, MBP^+ oligodendrocytes appeared to only be infected by CVS-11, while $OLIG2^+$ OPCs appeared to be infected by both viral strains. These findings highlight the relevance of the MyS model for investigating glia-virus interactions in a controlled, human-derived in vitro setting. Future studies should integrate sn/scRNAseq for better neurotropism studies.

There are some limitations to the MyS model that should be acknowledged. Unlike conventional brain organoids, MyS do not recapitulate the typical layered cortical architecture of the human cortex. Although the transcriptome of MyS-derived oligodendrocytes resembles adult transcriptional profiles more closely than oligodendrocytes described in other in vitro models, incomplete maturation remains a concern. Consistently, although the significant increase in cholesterol in week 15 MyS than in NMS as well as week 8 MyS suggest myelin maturation, the CE/PL ratio that remained low in week 15 MyS, suggest a more late fetal phenotype. In line with this, ultrastructural studies suggest a late fetal state of myelination, not yet an adult brain oligodendrocyte myelination phenotype. It is also possible that transcriptomic differences between MyS and in vivo oligodendrocytes may, in part, reflect in vitro culture-related artifacts. These could be further investigated by grafting iPSC-derived OPCs into in vivo models, as has been done for other neural cell types such as microglia. Further, we did not incorporate microglia in the MyS, where microglia are known to affect multiple aspects of brain development, including myelination [67]. In addition, microglia are critical regulators of remyelination, as demonstrated in lysolecithin-induced demyelination models where microglial activation and efficient clearance of myelin debris are required for oligodendrocyte differentiation and remyelination [9]. While the presence of maturing oligodendrocytes may contribute to electrophysiological maturation, variability between individual spheroids and spheroid slices remains incompletely understood and represents an additional limitation, necessitating complementary validation approaches. Finally, although our data suggest increased astrocyte generation in MyS, further validation beyond the current snRNA-seq analysis will be required to substantiate this observation.

Despite these limitations, the MyS model is a major advancement over current in vitro myelination models as a relatively fast and robust human-relevant myelination platform. It holds potential for the evaluation of compounds that promote oligodendrocyte differentiation and myelin repair. The cellular diversity present also provides opportunities to study cell-specific tropism in a tractable human model, with potential for extending this beyond RABV to other braintropic viruses; as well as anti-viral drug screens. Additionally, the MyS system is modular in design, allowing for disease modeling by mixing healthy and mutant NPCs or OPCs. This should make it possible to dissect cell-autonomous vs. non-cell-autonomous effects in de-myelinating disorders such as MS, and in other neurodegenerative disorders where defects in oligodendrocytes at least contribute to neurodegeneration [68].

Methodology

Culture of hPSCs

Two hPSC lines, Sigma-iPSC0028 (iPSC EPITHELIAL-1, Sigma, female, RRID: CVCL_EE38) and H9 embryonic stem cells (H9-ESCs) (WA09 WiCell research Institute, female, RRID: CVCL_9773) were used in this study. The hPSCs were genome engineered with an inducible transcription factor *SOX10* cassette in the Adeno-associated virus integration site 1 *(AAVS1)* locus via zinc finger nuclease gene editing to drive effective differentiation towards oligodendrocytes. hPSCs, with or without inducible *SOX10* (i*SOX10*) cassette were maintained on hESC qualified Matrigel (Corning) coated 6-well plates in E8 flex medium (E8 basal medium with E8 supplement flex and 1% penicillin/streptomycin (Gibco)). hPSCs were passaged twice a week with 0.5 mM ethylenediaminetetraacetic acid (EDTA). The cells were regularly tested for mycoplasma contamination using the MycoAlert Mycoplasma Detection Kit (Lonza).

Differentiation of hPSCs To Cortical NPCs

Cortical NPCs were generated following the protocol described by Shi et al. [69]. Sigma-iPSC0028 and H9-ESCs were cultured on Matrigel-coated 6-well plates (Corning) in mTESR (StemCell Technologies) with Revitacell (Life Technologies). hPSCs were allowed to proliferate to 90% confluency, dissociated into single cells by Accutase (Sigma) and seeded at 2.5 million cells per well of a 6-well plate in neural induction medium (NIM, Table S6). The medium was changed every day for 11 days. On day 12, the neuroepithelial cells were dissociated with Dispase II (Sigma), cultured for an additional 4 days with neuronal maintenance medium (NMM, Table S6) with 20 ng/mL basic fibroblast growth factor (bFGF) and purified by passaging rosette-forming neuroepithelial cells twice with Dispase II (one each after 5–7 days). NPCs were dissociated on day 33 with Accutase and cryopreserved in NMM complemented with 10% dimethyl sulfoxide (DMSO) (Sigma) for further experimental use.

Differentiation of hPSCs To OPCs

OPCs were generated by overexpression of the transcription factor *SOX10* in Sigma-iPSC0028 and H9-ESCs cell lines as described in Garcia et al. [70]. Briefly, Sigma-i*SOX10*-iPSC0028 iPSCs and i*SOX10*-H9-ESCs were cultured in E8 flex medium, dissociated with Accutase and plated at a density of 25,000 cells/cm^2 on a Matrigel-coated 6-well plate. After 1 day, oligodendrocyte induction medium (OIM, Table S6) was added for the following 6 days. On day 7, OIM containing 1 μM Sonic hedgehog agonist (SAG) was added and the medium was refreshed daily until day 11. Cells were then dissociated with Accutase and replated at 50,000–75,000 cells/cm^2 in the Basal Medium (Table S6) on poly-L-ornithin (PLO)-laminin coated 12-well plate to direct them towards oligodendrocyte fate. The medium was changed every day until day 23. On day 24, the cells were dissociated with Accutase and cryopreserved in the same medium with 15% DMSO for further experimental use.

Generation of NMS and MyS

Days in vitro (DIV) 33 cortical NPCs were thawed in NMM supplemented with Revitacell (Life Technologies) and maintained in culture for five days. On the day of sphere generation, DIV24 OPCs were thawed in NMM and DIV38 NPCs were dissociated with Accutase followed by cell counting by nucleocounter (ChemoMetec). 3D spheres were generated by diluting the cells in 2X NMM (NMM supplemented with 0.5X B27 (Gibco), 0.5X N2 (Gibco)), 20% KnockOut Serum Replacement and 1% methylcellulose (Sigma) and forming 30 μL droplets hanging onto the inside part of a turned-over lid of a petri dish. The 3D NMS and 3D MyS comprised of 90,000 DIV38 NPCs or 30,000 DIV38 NPCs with 60,000 DIV24 OPCs, respectively, per droplet. The hanging drops were carefully transferred to the incubator for 24 h, at which time the aggregated spheres were collected with a cut P1000 tip and transferred to 12-well ultra-low attachment plates (Corning) containing oligodendrocyte maturation medium (OMM, Table S6) supplemented with 3 μg/mL doxycycline for a week followed by only OMM. Plates were maintained on a rotating platform (IKA Wobble shakers Rocker 3D) on 50 revolutions per minute (rpm) for 6–15 weeks.

Quantification of Gene Expression by real-time Quantitative Polymerase Chain Reaction (RT-qPCR)

DIV 33 NPCs and DIV 24 OPCs monocultures were collected as a cell pellet respectively, and RNA extraction was performed by Quick-RNA Microprep Kit (Zymo research). The total amount of RNA was quantified using the NanoDrop system (Thermo Fisher Scientific) and 500 ng to1 µg RNA was used to prepare cDNA using SuperScript™ III First-Strand Synthesis System kit (Thermo Fisher Scientific). For 3D cultures, two spheroids of MyS or NMS were combined for each sample. RNA extraction, quantification and cDNA preparation were performed as mentioned above. RT-qPCR was performed to assess the expression of neuronal, astroglial and oligodendrocyte lineage markers by using Platinum SYBR Green qPCR Supermix-UDG (Thermo Fisher Scientific) on the ViiA 7 Real-Time PCR System (Applied Biosystems, USA). Analysis of gene expression was done by normalizing the cycle threshold (CT) value to that of the housekeeping gene Glyceraldehyde-3-phosphate dehydrogenase (GAPDH) and the delta CT was plotted. Primer sequences for each marker are listed in Table S7.

For Rabies virus (RABV) infected 3D MyS, RNA extracted from the culture supernatant (MACHEREY-NAGEL, cat 740956) was analyzed by RT-qPCR with iTaq™ Universal SYBR® Green One-Step Kit (BIO-RAD). Primers specific for RABV SAD-B19 and CVS-11 are listed in Table S7. The standard curve was generated from the RNA extracted from a 1/10 serial dilution series of a virus stock with known amount of infectious units of 3.6×10^7 $TCID_{50}$/mL (determined using end-point dilution and expressed as tissue culture infected dose 50% ($TCID_{50}$)). A 20 µL qPCR reaction comprised 4 µL of extracted RNA or standard, 10 µL of iTaq Universal SYBR® Green reaction mix, 0.25 µL of reverse transcriptase and 600 nM of each forward and reverse primer. RT-qPCR was performed on a QuantStudio 5 (Thermo Fisher Scientific) with the following protocol: 10 min (min) at 50 °C for reverse transcription, 1 min at 95 °C for polymerase activation and DNA denaturation, 40 cycles of 95 °C 15 s (s) and 62 °C 30 s for PCR amplification. Viral RNA copies were quantified based on the standard curve and are represented as $TCID_{50}$ equivalents/mL ($TCID_{50}{}^{eq}$/mL). The limit of quantification (LOQ) of viral RNA is defined by the lowest tested concentration from the standard curve that is still in the linear range.

Immunofluorescence Microscopy and Quantification of Cellular Composition of NMS and MyS

Week 10 MyS or NMS harvested were fixed in 4% paraformaldehyde (PFA) overnight at 4 °C. The next day, PFA was replaced with 30% sucrose followed by overnight incubation at 4 °C. Spheroids were collected using a cut P1000 tip and embedded in Optimal Cutting Temperature (OCT) compound by snap-freezing in liquid nitrogen. Cryosectioning was performed using a CryoStar NX70 (Thermo Fisher Scientific) to obtain 30 µm-thick sections, which were stored at −20 °C until use. For immunostaining, 3–6 sections per spheroid (one central and two peripheral) were selected. Sections were washed with phosphate-buffered saline (PBS), blocked and permeabilized using 0.5% Triton X-100 in PBS (PBST) supplemented with 5% normal goat serum (Dako) for 1 h at room temperature (RT). Samples were incubated with primary antibodies (Table S8) diluted in PBST overnight at 4 °C in humidified chambers, washed with PBS three times with 5 min interval, and secondary antibodies (species matched) diluted in Dako Real Antibody diluent were added for 1 h at RT. Samples were washed with 0.01% PBST, three times with 10 min interval, and nuclei were stained with Hoechst 33,342 (Sigma, 1:1000 dilution). Quantification of neurons, astrocytes, and oligodendrocytes was performed using QuPath software [71]. Cell types were identified based on marker-specific fluorescence intensity, and automated detection pipelines were used to segment and quantify positive cells within defined regions of interest (ROIs). Thresholds were optimized and kept constant to ensure comparability across samples.

RABV CVS-11 was kindly provided by Prof. Steven Van Gucht (Sciensano, Brussels, Belgium). RABV mCherry-SAD-B19 was kindly provided by the laboratory of Prof. Ashley C Banyard (Animal & Plant Health Agency, Surrey, UK). The mCherry sequence is inserted before the first gene within the genome of the SAD-B19 strain as described [72]. 3D MyS samples infected with RABV (CVS-11 or mCherry-SAD-B19) were sliced (30 µm thickness) using cryostat (Cryostar NX70, Thermo Fisher Scientific). The slices were incubated with an anti-RABV Nucleoprotein antibody (FITC Anti-Rabies Monoclonal Globulin (Table S8) diluted in PBST after nuclei staining for overnight at 4 °C, followed by thrice PBS washing. mCherry fluorescence was used as an indication for RABV infection in SAD-B19 (mCherry tagged) RABV infected 3D MyS samples (validated with the anti-RABV Nucleoprotein antibody in Figure S10). 3D MyS slices immunostained with cell type specific markers and/or RABV markers were mounted with ProLong Gold antifade mounting reagent (Life technologies). Confocal imaging was done using a Nikon C2 confocal microscope equipped with long-distance objective lens. 3D rendering images were made using the confocal images, afterwards using the VAA3D software (VAA3D-Neuron2_Autotracing) [73].

Transmission Electron Microscopy (TEM)

Spheroids were fixed in 2.5% glutaraldehyde (Electron Microscopy Services #16220) in 0.1 M sodium cacodylate buffer (Electron Microscopy Services #12300), pH 7.6 for 45 min on a shaker at 50 rpm at RT. Samples were washed thrice with 0.1 M sodium cacodylate buffer and 1% osmium tetra-oxide (Electron Microscopy Services #19151) with 1.5% potassium ferrocyanide (Sigma #455989) diluted in 0.1 M sodium cacodylate buffer was added. Samples were incubated for an hour at 4 °C on a shaker. The samples were washed with Milli-Q water six times at 2 min intervals, followed by overnight incubation in 2% Uranyl acetate (Electron Microscopy Services #22400) diluted in Milli-Q water at 4 °C. The next day, samples were washed five times for 7 min with Milli-Q water, before lead aspartate staining (Lead Nitrate- Electron Microscopy Services #17900 and L-aspartic acid-Sigma #11189, pH 5.5) for 30 min at 60 °C. Next, samples were washed with Milli-Q water thrice and dehydration was done by increasing concentrations of ethanol (30%, 50%, 70%, 90%, 100%) on ice, 10 min each. A second 100% ethanol step was done, followed by twice propylene oxide (Thermo Fisher Scientific #10487920) treatment for 10 min at RT. Spheroids were transferred to epon resin/propylene oxide mixtures before overnight infiltration with pure epon resin (Agar Scientific #AGR1081). The next day, the spheroids were embedded in inverted beam capsules and 70 nm thick slices were sectioned from the spheroids using the Leica Reichert Ultracut S2 and imaged using a JEM1400 transmission electron microscope (JEOL), operating at 80 kV and equipped with an Olympus SIS Quemesa 11MP camera.

Quantification of myelin sheets in a 70 nm sections, one from the periphery (around 50 nm from the surface) and one from the center (around 200 µm from the surface) of each spheroid was combined and considered as one biological replicate. More than 220 axons from both week 10 and week 15 MyS samples were manually quantified across three independent biological replicates to assess various myelin sheath parameters. Measurements including axon radius, myelin thickness, and the number of myelin lamellae were performed using ImageJ on TEM images. Myelinated axons were classified into three categories based on interlamellar spacing: loose (> 40 nm), mid-compact (15–40 nm), and compact (< 15 nm) myelin based on published literature [74] and empirical observations from our dataset. Interlamellar distance was quantified using higher-magnification images of myelinated neurons, with measurements obtained manually using ImageJ software. The G-ratio was calculated as the ratio of the inner axonal radius to the total outer radius (axon + myelin). Percentage for each myelin type was determined by dividing the number of axons in that category (loose, mid-compact or compact) by the total number of myelinated structures per biological replicate. Additionally, sections of 300 nm were cut with the Leica Reichert Ultracut S2 and tomograms were acquired using a Jeol 200 kV S/TEM JEM F200 electron microscope with cold Field Emission Gun. Tilt series were obtained by SerialEM with a step width of 3° from − 60° to 60° in STEM mode using a JEOL Bright Field detector. The 3D reconstruction was done with IMOD and the 3D representation with Amira software (Thermo Fisher Scientific, Video S1-2).

Lipidomics

NMS and MyS Spheroids were collected at weeks 8 and 15. The spheroids were homogenized in 800 µL water with a handheld sonicator, and an amount of homogenate containing 1 µg DNA was diluted with water to 700 µL and mixed with 800 µL 1 N HCl: CH_3OH 1:8 (v/v), 900 µL $CHCl_3$ and 200 µg/mL 2,6-di-tert-butyl-4-methylphenol (BHT; Sigma-Aldrich), 3 µL of SPLASH® LIPIDOMIX® Mass Spec Standard (Avanti Polar Lipids, 330707), and 3 µL of Ceramides and 3 µL of Hexosylceramides Internal Standards (cat. no. 5040167 and 5040398, AB SCIEX). The organic phase was rated and evaporated by Savant Speedvac spd111v (Thermo Fisher Scientific) at RT for 1–2 h. The remaining lipid pellets were stored at −80 °C for further use. For the DNA quantitation, a standard curve of herring sperm DNA concentrations in homogenization buffer (0.05 M $NaHPO_4$/NaHPO; buffer, 2.0 M NaCl, 2.10 M EDTA, pH 7.4) was made. 10 µL of the sample homogenates was mixed with homogenization buffer and incubated for an hour at 37 °C in dark. 1 µg/mL Hoechst dye (Calbiochem) was added to both standards and samples, and fluorescence was measured at excitation filter of 360–390 nm and an emission filter of 450–470 nm for determination of DNA concentrations. Samples were assessed on a liquid chromatography electrospray ionization tandem mass spectrometer (Nexera X2 UHPLC system (Shimadzu) coupled with 6500 + QTRAP system; AB SCIEX) to identify several lipid classes. All lipid species were measured with a scheduled Multiple Reaction Monitoring (MRM) method. Sphingomyelin, cholesterol esters, ceramides, hexose-ceramides, and lactose-ceramides were measured in positive ion mode with the MRM transitions being based on fragment losses m/z 184.1, 369.4, 264.4, 264.4, and 264.4, respectively. Triglycerides, diglycerides and monoglycerides were measured in positive ion mode with the transitions being based on the neutral loss of one of the fatty acyl moieties. Phosphatidylcholine, alkylphosphatidylcholine, alkenylphosphatidylcholine, lysophosphatidylcholine, phosphatidylethanolamine, alkylphosphatidylethanolamine, alkenylphosphatidylethanolamine, lyso phosphatidylethanolamine, phosphatidylglycerol, phosphatidylinositol, and phosphatidylserine were measured in negative ion mode with MRM transitions for the fatty acyl fragment ions.

Peak integration was performed with the MultiQuant™ software version 3.0.3. Lipid species signals were corrected for isotopic contributions (calculated with Python Molmass 2019.1.1). The total lipid amount and concentration per lipid class were expressed as absolute values in nmol/mg DNA. The lipidomic dataset was analyzed using the web-based application MetaboAnalyst 6.0 [75, 76]. Missing values were addressed through imputation. Lipid species with > 50% missing values were removed, and the remaining missing values were substituted with the lowest of detection imputation method (1/5 of the smallest positive value of each variable). Data were normalized with a $\log_{10}$ transformation, and a Pareto scaling was applied (mean-centered and divided by the square root of the standard deviation of each variable). A further step was performed using the EigenMS method to estimate batch effects and identify systematic biases [77]. This normalization method employs a combination of analysis of variance (ANOVA) and singular value decomposition applied to the residuals matrix to remove these biases. We also calculated false discovery rate (FDR)-corrected q values using the Benjamini-Hochberg procedure with an alpha level of 5% for each lipid class and subclass. Groups were compared using principal component analysis and hierarchical clustering heatmaps (distance measure: Euclidean, clustering algorithm: ward, standardization: auto-scale features).

Cholesterol Detection

Week 8 and 15 spheroids were collected, and lipids extracted by homogenizing the spheroids in 100 µL water with a handheld sonicator. DNA measurement was done by preparation of a standard curve of DNA measurements were done using Hoechst dye as mentioned above. Following DNA measurements, the samples were dehydrated using a speed-vacuum for an hour. The dry pellet was used for cholesterol measurement using the Cholesterol/Cholesteryl Ester Assay Kit (Abcam, #ab65359) according to the manufacturer's protocol. A total of 120 ng of DNA from each sample was used to measure cholesterol concentrations, and fluorescence was recorded using a 520 nm excitation and 580–640 nm emission filter.

Sample Preparation for single-nuclei RNA Sequencing (snRNAseq)

For nuclei isolation, all steps were done on ice with precooled buffers, and centrifugation was maintained at 4 °C. Briefly, week 8 or 15 old NMS and MyS (4–6 spheroids per sample) were transferred to 250 µL of ice-cold homogenization buffer (HB; 10 mM Tris pH 7.8, 0.1 mM EDTA, 320 mM sucrose, 5 mM $CaCl_2$, 3 mM magnesium acetate, 0.1% NP40, 1X complete protease inhibitor (Roche), 1 mM β-mercaptoethanol, and RNase inhibitor (Promega)) for 3 min to preserve nuclear integrity. Samples were gently homogenized using pestle A (5 strokes) followed by pestle B (15 strokes) and the homogenates were passed through 70 µm EASYstrainer (Greiner). The homogenizer and the strainer were washed with additional 270 µL of HB, and 520 µL of gradient medium (10 mM Tris pH 7.8, 5 mM $CaCl_2$, 50% Optiprep, 3 mM magnesium acetate, 1X complete protease inhibitor, 1 mM β-mercaptoethanol, and RNase inhibitor) was added to the samples. This solution was carefully layered onto a cushion solution (29% Optiprep, 150 mM KCl, 30 mM $MgCl_2$, 60 mM Tris pH 7.8, and 250 mM sucrose) and centrifuged at 9000 rpm for 25 min at 4 °C. The supernatant was discarded carefully, and nuclei pellets were then resuspended in 25 µL of resuspension buffer (1X PBS, 2% bovine serum albumin (BSA)), filtered through Flowmi 40 µm cell strainers, and counted using a LUNA automated cell counter (Logos Biosystems) following the manufacturer's instructions. The diluted nuclei suspensions were subsequently loaded onto the 10X Chromium Single Cell Platform (10X Genomics) (Next GEM Single Cell 3′ library and Gel Bead Kit v3.1) in accordance with the manufacturer's protocol (10X User Guide; CG000315, Revision E). Steps including generation of gel beads in emulsion (GEMs), barcoding, GEM-RT cleanup, complementary DNA amplification, and library construction were all performed according to protocol. The quality of individual samples was checked with a Fragment Analyzer (Agilent), and library quantification was done using Qubit 4.0 (Thermo Fisher Scientific) before pooling the libraries. The final pooled library was sequenced on a NovaSeq6000 (Illumina) instrument at the VIB Nucleomics Core, using the Illumina NovaSeq 6000 v1.5 sequencing kit S4 200 paired-end reads (28-10-10–90), 1% PhiX with 100-base-pair paired-end reads.

Quality control, snRNAseq Data pre-processing

The Cell Ranger pipeline (version 7.1.0, 10x Genomics) was employed for sample demultiplexing and the generation of FASTQ files for read 1, read 2, and the i7 sample index of the gene expression library. Read 2 sequences from the gene expression libraries were aligned to the reference genome (Human GRCh38 (GENCODE v32/Ensembl98) using the STAR aligner through CellRanger. Subsequent processing steps, including barcode processing, filtering of unique molecular identifiers (UMIs), and gene counting, were conducted using the Cell Ranger suite version 7.1.0.

Normalization, clustering, and Differential Gene Expression Analysis of snRNAseq Data

The gene count matrix for each sample was processed to exclude nuclei with fewer than 200 expressed genes and genes expressed in fewer than 3 nuclei. Additionally, quality control was performed using the Scater package (Version 1.32.1), both univariately and multivariately. This involved filtering out nuclei with extremely low or high total counts/transcripts (library size) (median absolute deviations (MAD) of 5), nuclei with low or high numbers of expressed genes (MAD of 5), and nuclei with a very high percentage of mitochondrial transcripts (MAD of 15). We used the Seurat pipeline (Seurat package, version 5.0.3) for normalization, scaling, and clustering. A Seurat object was constructed for each individual sample from the counts and metadata, followed by log-normalization of the count matrix. The most highly variable genes (HVGs) were identified using the FindVariableFeatures function with default parameters. To capture the primary sources of variability, the data was scaled, and 50 principal components (PCs) were computed from the scaled normalized counts of overdispersed genes via PCA analysis (using the RunPCA function with default settings). The number of PCs were selected for each sample individually. The nearest neighbors (using the FindNeighbors function with default parameters) was then identified and a Shared Nearest Neighbors (SNN) graph with a resolution of 0.8 (using the FindClusters function with default parameters) was constructed to detect cell clusters. Subsequently, the Seurat objects from each individual sample were combined using the merge function with default settings (SeuratObject, version 5.0.1). The combined data underwent normalization, identification of HVGs, and scaling. Following this, PCA analysis was conducted, nearest neighbors were identified, and finally the clusters were determined by generating an SNN graph with a resolution of 0.5, as described above. The result of analysis was then visualized using Uniform Manifold Approximation and Projection (UMAP) on the first 30 PCs with the RunUMAP function. Finally, the FindAllMarkers function was employed to identify differentially expressed genes (DEGs) within each cluster, using the following parameters: min.pct = 0.01, min.cells.feature = 3, min.cells.group = 3, logfc.threshold = 0.2, min.diff.pct = 0.2, and test.use = "wilcox". For downstream enrichment analysis, only DEGs with a p-value < 0.05 were selected. Additionally, after determining the identity of each cluster, the FindMarkers function was employed to identify DEGs between clusters from coculture and monoculture conditions at 8-week and 15-week time points, separately. The analysis was conducted using the following parameters: min.pct = 0.25, min.cells.feature = 3, min.cells.group = 3, logfc.threshold = 0.25, min.diff.pct = -Inf, and test.use = "wilcox".

Differentially Expressed Genes (DEGs) and Gene Ontology (GO) Enrichment Analyses

DEGs across all clusters (adjusted p-value < 0.05 and $\log_2$ fold change > 0.2) were identified using Seurat's FindAllMarkers function, with p-values adjusted for multiple testing using Bonferroni correction. DEGs in oligodendrocyte and OPC populations between NMS and MyS at weeks 8 and 15 (adjusted p-value < 0.05 and $\log_2$ fold change > 1) were identified using Seurat's FindMarkers function, with p-values adjusted using Bonferroni correction. To verify the identity of each cluster, we performed GO enrichment analysis on the list of upregulated genes in each cluster using the Biological Process gene set library (p-values < 0.05). Additionally, cell type enrichment analysis was carried out using the CellMarker 2024 database (p-values < 0.05). All analyses were performed through the Enrichr database [78] (https://maayanlab.cloud/Enrichr/).

Integration Analysis

To evaluate the similarity of cell clusters from the MyS and NMS model to their in vivo counterparts or to other established iPSC-derived in vitro models, we integrated our data with several developing (Fetal_1: Yu et al.[35]; Fetal_2: Jessa et al.[36]) and adult [37–39, 79] (Adult_1: Allen Institute for Brain Science (https://brain-map.org/our-research/cell-types-taxonomies/cell-types-database-rna-seq-data/human-m1-10x) Bakken et al.[79,80]; Adult_2: Garcia et al. [39]; Adult_3: Lake et al.[38]) human brain single-nucleus/single-cell RNA sequencing (sn/scRNAseq) datasets as well as two in vitro [16, 19] *(In vitro*_1: Marton et al.[19]; In vitro_2: Fagiani et al.[16]) models containing oligodendrocytes and OPCs. In the dataset from Fagiani et al. [16], we specifically included samples that were treated with doxycycline but not with cerebrospinal fluid, encompassing both healthy and diseased samples. The integration of datasets was conducted using the merge function with default settings. The combined dataset was normalized, and HVGs were identified and scaled. PCA analysis was then performed, and nearest neighbors were identified based on the first 30 PCs. An SNN graph was constructed with a resolution of 0.5 to identify cell clusters. For batch correction, anchors between clusters were identified using the FindIntegrationAnchors function, employing the first 30 dimensions (Seurat package, version 5.0.3). These anchors were then used to integrate the datasets through IntegrateData function using default settings. The integrated data was normalized, and HVGs were identified and scaled. Next, the PCA analysis was done, clusters were identified and the SNN graph was generated as described above. Finally, the clusters were visualized using UMAP on the first 30 PCs with the RunUMAP function, as previously described. The resulting object was subsequently used for downstream analysis.

To assess the transcriptional similarity of oligodendrocyte populations across datasets, we performed a correlation analysis. As fetal brain datasets from 9 to 12 and 20-week-old fetuses lacked sufficient cells assignable to the oligodendrocyte cluster [35, 36], they were excluded from the analysis. For the remaining datasets, the AverageExpression function was used to calculate mean RNA expression values from the merged dataset to construct the correlation matrix. Top scoring features were subsequently selected using the SelectIntegrationFeatures function. The Spearman correlation was then determined on the processed data using the cor function. Finally, the correlation plot was generated utilizing the corrplot function from the corrplot package (version 0.95) [81]. To compare pseudobulk profiles of cell clusters from individual datasets within the merged dataset, the AggregateExpression function was employed (Seurat package, version 5.0.3). Subsequently, scatter plots were generated using the CellScatter function to visualize the expression levels of oligodendrocyte cell clusters across different datasets, with the myelin basic protein (MBP) specifically highlighted (Seurat package, version 5.0.3).

SlingShot Trajectory Inference Analysis

For trajectory inference, the batch-corrected dataset encompassing all datasets was utilized. The oligodendrocyte and fetal OPC clusters were subsetted using the Seurat package (version 5.0.3). Subsequently, trajectory analysis was conducted using the Slingshot package (version 2.12.0) [82], with the OPC cluster from the youngest fetal sample [35] designated as the root population.

RNA Velocity Analysis

To investigate transcriptional dynamics and forecast cell fate decisions, we conducted RNA velocity analysis on a distinct differentiating path, including progenitor, proliferating OPC, OPC, and oligodendrocyte populations, for MyS model at 8- and 15-week time point. The RNA velocity analysis was executed using the Python package scVelo (0.3.2), following the guidelines established by Bergen et al. (2020) [40] (https://scvelo.readthedocs.io/). Initially, clusters of interest were subsetted from the merged Seurat object of our snRNAseq data and converted to anndata format. The velocity command line tool was employed to calculate the spliced and unspliced counts matrix from the CellRanger output directory. Subsequently, the velocity was computed using the “dynamical mode”.

Electrophysiology

MyS and NMS were harvested on week 8–10 and embedded in 2% low melting agarose (Sigma) diluted in PBS supplemented with 137 mM NaCl, 2.7 mM KCl, 10 mM Na_2PO_4, 1.8 mM KH_2PO_4, pH = 7.4. The embedding of the spheroids was done on ice and the solidified agarose containing spheroids were sectioned at a thickness of 300 µm, using Leica VT1200S vibratome in ice-cold oxygenated (95% O_2 and 5% CO_2) artificial cerebrospinal fluid solution, composed of 127 mM NaCl, 25 mM $NaHCO_3$, 1.25 mM NaH_2 PO_4, 2.5 mM KCl, 1 mM $MgCl_2$, 2 mM $CaCl_2$, and 25 mM glucose. 2–3 sections from each spheroid (MyS or NM) were collected in 10 cm cell culture dish in NMM and the agarose was peeled off using a sharp blade under the microscope placed in a sterile culture hood. The spheroid slices of either MyS or NM were plated using a cut P1000 tip in one well each of high density multielectrode array (HD-MEA) 6 well plates (Maxwell Biosystems) coated with PLO-laminin. Excess NMM was carefully removed using SUGI absorption spears (AgnThos) while not disturbing the spheroid slices, and the slices were allowed to settle for a minute. 30 µL NMM supplemented with laminin was added very carefully, without disturbing the attachment of the spheroid slices in the well. These steps were repeated for all six wells and the HD-MEA plate was placed at 37 °C, 5% CO_2 for 1–2 h. Next, 150 µL medium was added to each well while avoiding disturbing the spheroid slices and the plates were returned to the incubator. The medium was changed on the following day with 150–200 mL OMM, followed by medium changes every other day. One day before the recording, OMM was replaced with BrainPhyS medium (Stemcell Technologies) and after the recording, BrainPhys was replaced with OMM. Spiking and bursting activity were recorded on a HD-MEA plate reader (Maxwell Biosystems) maintained at 37 °C and 5% CO_2.

Whole-sample electrical recordings were obtained using the Activity Scan Assay. Recordings (MaxLab Live) were conducted for 30 s per configuration. Spike times were extracted online using a threshold set at five standard deviations above the noise level. The high density of electrodes allowed precise identification and tracking of electrical activity in the MyS spheres for up to nine weeks post-plating. Wells were excluded from further analysis if threshold of 150 active electrodes with a firing rate (FR) of at least 1 Hz was not met, at any point during the recording period. The firing rate was calculated as the total number of spikes per electrode, normalized by the duration of the experiment.

For burst detection, an inter-spike interval (ISI)-based method was used. Bursts were defined as sequences of at least four consecutive spikes with ISIs of less than 50 milliseconds. Additionally, the total number of active electrodes (defined as electrodes with a firing rate of at least 0.1 Hz) were calculated. Only active electrodes were used to compute the firing rate, inter-spike interval, burst rate, and inter-burst interval. All metrics were averaged across electrodes associated with each sphere half. Electrodes belonging to a sphere half were assigned based on the electrical map of firing rates generated at week 7, 8 or 9. If two distinct spheres were visually identifiable, active electrodes were manually assigned to each sphere and counted as two independent technical replicates. In cases where only one sphere was visible, all electrodes were attributed to that sphere. This method allowed us to distinguish the activity and maturation of individual sphere halves, as shown in Figure S8b. As the sphere halves exhibited distinct trends in electrophysiological activity over time, we further quantified these patterns by separating the number of spheres showing increased, decreased, or maintained activity levels. Activity between week 4 and 8 in vitro was compared, with spheres classified as ‘increasing’ if they demonstrated at least a 30% rise in the number of active electrodes during this period, ‘decreasing’ if they showed a 30% decrease and ‘maintained’ otherwise.

Lysolecithin Treatment

Spheroids were incubated with lysolecithin (0.25 mg/mL, dissolved in OMM) for 15 h in a 12 well plate on a shaker at 50 rpm, 37 °C and 5% CO_2. Following lysolecithin treatment, spheroids were washed twice with PBS, resuspended in OMM, and returned to the shaker at 37 °C with 5% CO_2 for 3 h. Spheroids were collected with cut P1000 tip and transferred to 96-well plate containing 4% PFA for overnight incubation at 4 °C. The samples were processed for immunofluorescence staining and TEM as described.

RABV Infection of MyS

Week 10 MyS were distributed in 96-well plates, with one spheroid per well. RABV mCherry-SAD-B19 or CVS-11 strains (30/100/300 TCID50 per spheroid) were added and incubated with the MyS for 24 h. After incubation, the spheroids were washed 3 times with PBS, 300 µL fresh medium was added and the spheroids were further cultured. On day 1 and 4 post-infection, 150 µL cell culture supernatants from each well were collected for RT-qPCR analysis, and 200 µL fresh medium was added to each well to restore the volume. On day 6 post-infection, all culture medium were removed, spheroids were washed 3 times with PBS and fixed with 4% PFA at 4 °C overnight.

Statistical Analysis

The number of biological (N) and technical (n) replicates is mentioned in the respective figure legends. N represents biological replicates, corresponding to mostly independent experiments, whereas n denotes technical replicates, including the number of spheroids, spheroid slices, or qRT-PCR wells analyzed. Summary of all the experiments with the number of replicates (N = biological, n = technical) and cell line used are mentioned in Table S9. Statistical analyses were performed using Prism v.8.2.1 (GraphPad). Tests used include two-way ANOVA with Sidak’s multiple comparisons test, one-way ANOVA with Sidak’s multiple comparisons test, paired and unpaired two-tailed t-tests. Differences were considered statistically significant for two-sided p-values < 0.05 ($*p < 0.05$; $**p < 0.01$; $***p < 0.001$; $****p < 0.0001$).

Supplementary Information The online version contains supplementary material available at https://doi.org/10.1007/s12015-026-11061-4.

Acknowledgements The authors gratefully acknowledge the VIB Bio Imaging Core (LIMONE) and KU Leuven Core facility financing for their support and assistance in this work. The computational resources and services used in this work were provided by the VSC (Flemish Supercomputer Center), funded by FWO and the Flemish Government.

Author Contributions KA designed and performed experiments, analyzed data and wrote the manuscript. RR, XW, CV, DJ, JN, YCC designed the experiments, helped with coordinating the study and contributed in manuscript editing. TB, GAm, SP, KN, AS, GAr, EEC, FN, JT, KW, KV, NVD, SKP helped in the data analysis and edited the manuscript. IL, JS, LVDB, LDG, LM contributed in manuscript editing.

Funding This study was supported by the Research Foundation Flanders (FWO), including individual ongoing fellowships to K.A. (1S03424N) and T.B. (12AIK24N), and project grants to Y.C.C., C.V., K.A., R.R., F.N., J.T., E.E.C., K.N. (FWO-SBO-S001221N, OrganID and FWO-G0B5819N). Additional support was provided by the Mitialto Foundation.

Data Availability The main data supporting the findings of this study are available within the paper and its Supplementary Information. The datasets from the quantitative analysis generated during this study including source data and the data used to make figures as well as all the images are too large to be publicly shared. The data can be available for research purposes from the corresponding author on reasonable request. The raw data files for the single nuclei transcriptomics have been submitted in Gene Expression Omnibus and pending for the approval.

Declarations

Consent to Participate Not applicable.

Consent to Publish Not applicable.

Conflict of interest The authors declare no conflict of interest.

Competing interests The authors declare no competing interests.

Clinical Trial Number Not applicable.

References

1. Morell, P., & Quarles, R. H. (1999). The Myelin Sheath.
2. Staugaitis, S. M., & Trapp, B. D. (2012). Diseases Involving Myelin. *Basic Neurochem.* (p. 691). https://doi.org/10.1016/B978-0-12-374947-5.00039-0
3. Murayama, R., Cai, Y., Nakamura, H., & Hashimoto, K. (2025). Demyelination in psychiatric and neurological disorders: Mechanisms, clinical impact, and novel therapeutic strategies. *Neuroscience and Biobehavioral Reviews, 174*, Article 106209.
4. Gargareta, V. I., et al. (2022). Conservation and divergence of Myelin proteome and oligodendrocyte transcriptome profiles between humans and mice. *Elife*, *11*, e77019.
5. Zhou, W., et al. (2025). Critical analysis of translational potential of rodent models of white matter pathology across a wide spectrum of human diseases. *Cell Death and Disease*, *161*(16), 580. (2025).
6. Gargareta, V. I. (2022). Conservation and divergence of myelin proteome and oligodendrocyte transcriptome profiles between humans and mice. *Elife* 11.
7. Chrast, R., Saher, G., Nave, K. A., & Verheijen, M. H. G. (2011). Lipid metabolism in myelinating glial cells: Lessons from human inherited disorders and mouse models. *Journal of Lipid Research*, *52*, 419–434.
8. Piekarski, D. J., et al. (2023). White matter microstructural integrity continues to develop from adolescence to young adulthood in mice and humans: Same phenotype, different mechanism. *Neuroimage: Reports*, *3*, 100179.
9. Lange, S. (2025). Human myelinated brain organoids with integrated microglia as a model for myelin repair and remyelinating therapies. *Science Translational Medicine*. https://doi.org/10.1126/scitranslmed.adp7047
10. Hendriks, D., et al. (2024). Human fetal brain self-organizes into long-term expanding organoids. *Cell, 187*, 712-732.e38.
11. Shaker, M. R. (2021). Rapid and efficient generation of myelinating human oligodendrocytes in organoids. *Front Cell Neurosci* 15.
12. Kim, H., & Jiang, P. (2021). Generation of human pluripotent stem cell-derived fused organoids with oligodendroglia and myelin. *STAR Protocols*. https://doi.org/10.1016/j.xpro.2021.100443
13. James, O. G., et al. (2021). iPSC-derived myelinoids to study myelin biology of humans. *Developmental Cell, 56*, 1346-1358.e6.
14. Marton, R. M., et al. (2019). Differentiation and maturation of oligodendrocytes in human three-dimensional neural cultures. *Nature Neuroscience, 22*, 484.
15. Madhavan, M., et al. (2018). Induction of myelinating oligodendrocytes in human cortical spheroids. *Nature Methods, 15*, 700–706.
16. Fagiani, F. (2024). A glia-enriched stem cell 3D model of the human brain mimics the glial-immune neurodegenerative phenotypes of multiple sclerosis. *Cell Reports Medicine*. https://doi.org/10.1016/j.xcrm.2024.101680
17. Feng, L. (2023). Developing a human iPSC-derived three-dimensional myelin spheroid platform for modeling myelin diseases. *IScience*. https://doi.org/10.1016/j.isci.2023.108037
18. van Tilborg, E., et al. (2017). Origin and dynamics of oligodendrocytes in the developing brain: Implications for perinatal white matter injury. *Glia, 66*, 221.
19. Marton, R. M. (2019). Differentiation and Maturation of Oligodendrocytes in Human Three-Dimensional Neural Cultures. *Nat Neurosci* 22. https://doi.org/10.1038/s41593-018-0316-9
20. Miyazaki, Y., et al. (2024). Oligodendrocyte-derived LGI3 and its receptor ADAM23 organize juxtaparanodal Kv1 channel clustering for short-term synaptic plasticity. *Cell Reports, 43*, Article 113634.
21. Zhou, L. (2020). Gab1 mediates PDGF signaling and is essential to oligodendrocyte differentiation and CNS myelination. *Elife* 9.
22. Santra, M., et al. (2014). Thymosin β4 up-regulation of MicroRNA-146a promotes oligodendrocyte differentiation and suppression of the toll-like proinflammatory pathway. *Journal of Biological Chemistry, 289*, 19508.
23. Wang, P., et al. (2021). Predicting signaling pathways regulating demyelination in a rat model of lithium-pilocarpine-induced acute epilepsy: A proteomics study. *International Journal of Biological Macromolecules, 193*, 1457–1470.
24. Chapman, T. W., Piedra, E. T., & Hill, R. A. Oligodendrocyte maturation alters the cell death mechanisms that cause demyelination. https://doi.org/10.1101/2023.09.26.557781
25. Chamling, X., et al. (2020). Single-Cell transcriptomic analysis reveals molecular diversity of human oligodendrocyte progenitor cells. *BioRxiv*, *2020.10.07.328971*. https://doi.org/10.1101/2020.10.07.328971
26. Ji, K., Ren, H., Zhao, X., & Yan, C. (2022). Migratory rolandic encephalopathy caused by the mitochondrial ND3 variant. *Neurology, 98*, 80–81.
27. Hassel, L. A., et al. (2023). Differential activity of transcription factor Sox9 in early and adult oligodendroglial progenitor cells. *Glia, 71*, 1890–1905.
28. Braccioli, L., Vervoort, S. J., Puma, G., Nijboer, C. H., & Coffer, P. J. (2018). SOX4 inhibits oligodendrocyte differentiation of embryonic neural stem cells in vitro by inducing Hes5 expression. *Stem Cell Research, 33*, 110–119.
29. Wang, Y. (2021). PARP1-mediated parylation activity is essential for oligodendroglial differentiation and CNS myelination. *Cell Rep* 37.
30. Yaffe, Y., et al. (2015). The myelin proteolipid plasmolipin forms oligomers and induces liquid-ordered membranes in the Golgi complex. *Journal of Cell Science, 128*, 2293–2302.
31. Reza, S., Ugorski, M., & Suchański, J. (2021). Glucosylceramide and galactosylceramide, small glycosphingolipids with significant impact on health and disease. *Glycobiology*, *31*, 1416.
32. Huang, H., et al. (2017). Tmeff2 is expressed in differentiating oligodendrocytes but dispensable for their differentiation in vivo. *Scientific Reports, 7*(1), 1–8.
33. Filippini, A. (2024). Leucine-Rich Repeat Kinase-2 Controls the Differentiation and Maturation of Oligodendrocytes in Mice and Zebrafish. *Biomolecules* 14.

34. Lin, J. P., Mironova, Y. A., Shrager, P., & Giger, R. J. (2017). LRP1 regulates peroxisome biogenesis and cholesterol homeostasis in oligodendrocytes and is required for proper CNS myelin development and repair. *eLife, 6*, Article e30498.
35. Yu, Y. (2021 2412). Interneuron origin and molecular diversity in the human fetal brain. *Nat. Neurosci.* 24, 1745–1756 (2021).
36. Jessa, S., et al. (2019). Stalled developmental programs at the root of pediatric brain tumors. *Nature Genetics, 51*(12), 1702–1713.
37. Bakken, T. E., et al. (2021). Comparative cellular analysis of motor cortex in human, marmoset and mouse. *Nat 2021 5987879, 598*, 111–119.
38. Lake, B. B., et al. (2017). Integrative single-cell analysis of transcriptional and epigenetic states in the human adult brain. *Nature Biotechnology, 36*(1), 70–80.
39. Garcia, F. J., et al. (2022). Single-cell dissection of the human brain vasculature. *Nature, 603*(7903), 893–899.
40. Bergen, V., Lange, M., Peidli, S., Wolf, F. A., & Theis, F. J. (2020). Generalizing RNA velocity to transient cell states through dynamical modeling. *Nature Biotechnology, 38*(12), 1408–1414.
41. Vana, N. S., et al. (2023). Early cortical oligodendrocyte precursor cells are transcriptionally distinct and lack synaptic connections. *Glia, 71*, 2210–2233.
42. Khawaja, R. R., et al. (2021). GluA2 overexpression in oligodendrocyte progenitors promotes postinjury oligodendrocyte regeneration. *Cell Reports, 35*, Article 109147.
43. Fard, M. K. (2017). BCAS1 expression defines a population of early myelinating oligodendrocytes in multiple sclerosis lesions. *Sci Transl Med* 9.
44. Kim, D., An, H., Fan, C., & Park, Y. (2021). Identifying oligodendrocyte enhancers governing Plp1 expression. *Human Molecular Genetics*, *30*, 2225–2239.
45. Fulton, D., Paez, P. M., & Campagnoni, A. T. (2010). The multiple roles of myelin protein genes during the development of the oligodendrocyte. *ASN Neuro, 2*, Article e00027.
46. Kaneko, N., et al. (2024). ADAMTS2 promotes radial migration by activating TGF-β signaling in the developing neocortex. *Embo Reports*, *25*, 3090–3115.
47. Fitzner, D., et al. (2020). Cell-type- and brain-region-resolved mouse brain lipidome. *Cell Reports, 32*, Article 108132.
48. Dawson, G. (2015). Measuring brain lipids. *Biochimica et Biophysica Acta, 1851*, 1026–1039.
49. O'Brien, J. S., & Sampson, E. L. (1965). Lipid composition of the normal human brain: Gray matter, white matter, and myelin. *Journal of Lipid Research, 6*, 537–544.
50. Oliveira, M., et al. (2022). Early life to adult brain lipidome dynamic: A Temporospatial study investigating dietary polar lipid supplementation efficacy. *Frontiers in Nutrition, 9*, Article 898655.
51. Saher, G., et al. (2005). High cholesterol level is essential for myelin membrane growth. *Nature Neuroscience, 8*(4), 468–475.
52. Berghoff, S. A., et al. (2021). Neuronal cholesterol synthesis is essential for repair of chronically demyelinated lesions in mice. *Cell Reports, 37*, Article 109889.
53. Birgbauer, E., Rao, T. S., & Webb, M. (2004). Lysolecithin induces demyelination in vitro in a cerebellar slice culture system. *Journal of Neuroscience Research*, *78*, 157–166.
54. Morecki, R., & Zimmerman, H. M. (1969). Human rabies encephalitis: Fine structure study of cytoplasmic inclusions. *Archives of Neurology*, *20*, 599–604.
55. Matsumoto, S. (1963). Electron microscope studies of rabies virus in mouse brain. *The Journal of Cell Biology, 19*, 565–591.
56. Harsha, P. K., et al. (2022). Mitochondrial dysfunction in rabies virus-infected human and canine brains. *Neurochemical Research, 47*, 1610–1636.
57. Li, X. Q., Sarmento, L., & Fu, Z. F. (2005). Degeneration of neuronal processes after infection with pathogenic, but not attenuated, rabies viruses. *Journal of Virology, 79*, 10063–10068.
58. Giussani, P., Prinetti, A., & Tringali, C. (2021). The role of sphingolipids in myelination and myelin stability and their involvement in childhood and adult demyelinating disorders. *Journal of Neurochemistry, 156*, 403–414.
59. Stikov, N., et al. (2015). In vivo histology of the myelin g-ratio with magnetic resonance imaging. *NeuroImage, 118*, 397–405.
60. Bouhrara, M., et al. (2021). Age-related estimates of aggregate g-ratio of white matter structures assessed using quantitative magnetic resonance neuroimaging. *Human Brain Mapping, 42*, 2362–2373.
61. Peters, A., Palay, S. L., & Webster, H. (1976). deF. The Fine Structure of the Nervous System: neurons and their supporting cells. xviii, 494.
62. Tsiang, H., Koulakoff, A., Bizzini, B., & Berwald-Netter, Y. (1983). Neurotropism of rabies virus. An in vitro study. *Journal of Neuropathology and Experimental Neurology*, *42*, 439–452.
63. Potratz, M., et al. (2020). Astrocyte infection during Rabies encephalitis depends on the virus strain and infection route as demonstrated by novel quantitative 3D analysis of cell tropism. *Cells, 9*, Article 412.
64. Potratz, M., et al. (2020). Neuroglia infection by rabies virus after anterograde virus spread in peripheral neurons. *Acta Neuropathologica Communications, 8*, Article 199.
65. Jenson, A. B., Rabin, E. R., Bentinck, D. C., & Melnick, J. L. (1969). Rabiesvirus neuronitis. *Journal of Virology, 3*, 265–269.
66. Murphy, F. A., Bauer, S. P., Harrison, A. K., & Winn, W. C. (1973). Comparative pathogenesis of rabies and rabies-like viruses. Viral infection and transit from inoculation site to the central nervous system. *Laboratory Investigation, 28*, 361–376.
67. McNamara, N. B., et al. (2022). Microglia regulate central nervous system Myelin growth and integrity. *Nat 2022 6137942*, *613*, 120–129.
68. Garton, T., Gadani, S. P., Gill, A. J., & Calabresi, P. A. (2024). Neurodegeneration and demyelination in multiple sclerosis. *Neuron, 112*, 3231–3251.
69. Shi, Y., Kirwan, P., & Livesey, F. J. (2012 710). Directed differentiation of human pluripotent stem cells to cerebral cortex neurons and neural networks. *Nat. Protoc.* 7, 1836–1846 (2012).
70. García-León, J. A., et al. (2020). Generation of oligodendrocytes and establishment of an all-human myelinating platform from human pluripotent stem cells. *Nature Protocols, 15*, 3716–3744.
71. Morriss, N. J., et al. (2020). Automated quantification of immunohistochemical staining of large animal brain tissue using QuPath software. *Neuroscience, 429*, 235–244.
72. Wu, G. (2023). A simplified method for measuring neutralising antibodies against rabies virus. *J Virol Methods* 319.
73. Peng, H., Bria, A., Zhou, Z., Iannello, G., & Long, F. (2013 91). Extensible visualization and analysis for multidimensional images using Vaa3D. *Nat. Protoc.* 9, 193–208 (2014).
74. Scherer, S. S. (1997). Molecular genetics of demyelination: New wrinkles on an old membrane. *Neuron, 18*, 13–16.
75. Pang, Z., et al. (2024). MetaboAnalyst 6.0: Towards a unified platform for metabolomics data processing, analysis and interpretation. *Nucleic Acids Research, 52*, W398–W406.
76. Ewald, J. D., et al. (2024). Web-based multi-omics integration using the Analyst software suite. *Nature Protocols, 19*, 1467–1497.

77. Karpievitch, Y. V., Nikolic, S. B., Wilson, R., Sharman, J. E., & Edwards, L. M. (2014). Metabolomics data normalization with EigenMS. *PLoS One, 9*, Article e116221.
78. Chen, E. Y., et al. (2013). Enrichr: Interactive and collaborative HTML5 gene list enrichment analysis tool. *Bmc Bioinformatics*, *14*, 1–14.
79. Human M1 10x https://brain-map.org/our-research/cell-types-taxonomies/cell-types-database-rna-seq-data/human-m1-10x
80. Bakken, T. E., et al. (2021). Comparative cellular analysis of motor cortex in human, marmoset and mouse. *Nature*, *598*, 111–119.
81. Friendly, M. (2002). Corrgrams. *The American Statistician, 56*, 316–324.
82. Street, K., et al. (2018). Slingshot: Cell lineage and pseudotime inference for single-cell transcriptomics. *Bmc Genomics*, *19*, 1–16.